Short-lived flashes of gamma radiation in a quasi-spherical Szekeres metric

Andrzej Krasiński

N. Copernicus Astronomical Centre,
Polish Academy of Sciences,
Bartycka 18, 00 716 Warszawa, Poland[*]

(Dated:)

In previous papers it was shown that gamma rays with characteristics similar to those of the gamma-ray bursts (GRBs) observed by astronomers may arise from suitably shaped nonuniformities in the Big Bang in a quasi-spherical Szekeres (QSS) model. The gamma radiation arises by blueshifting the light emitted by hydrogen atoms at the end of the last scattering epoch along preferred directions that exist in QSS models. However, the durations of the gamma flashes and of their afterglows implied by the model were much longer than those of the observed GRBs. In this paper it is shown that durations of the correct order result if the blueshifted radiation, on its way to the present observer, passes through another QSS region where it is deflected. The angle of deflection changes with time because of the cosmological drift mechanism, so the high-frequency ray will miss the observer after a while. It is shown by explicit numerical calculation that a gamma-ray flash will no longer be visible to the present observer after 10 minutes.

I. MOTIVATION AND BACKGROUND

In previous papers by this author [1–3] it was shown that flashes of gamma radiation with characteristics similar to those of the gamma-ray bursts (GRBs), now routinely observed by astronomers [4], may arise from a non-simultaneous Big Bang (BB) in a quasi-spherical Szekeres (QSS) model [5–7]. The gamma radiation arises by blueshifting the light emitted by hydrogen atoms at the end of the last scattering epoch along preferred directions existing in QSS models [2, 3] (for the first discussions of blueshifting see Refs. [8, 9]). With the BB profile $t_B(r)$ chosen suitably, the blueshift is sufficiently strong to move the observed frequency of the radiation to the gamma range. A multitude of sources can be created by distributing small QSS regions over a Friedmann background [3]. However, the durations of the gamma flashes and of their afterglows implied by the model were much longer than those measured for the GRBs.

In this paper it is shown that durations of the correct order result if the blueshifted radiation, on its way to the present observer, passes through another QSS region, where it is deflected. The angle of deflection changes with time in consequence of the cosmic drift [10–12], so the high-frequency ray will miss the observer after a while.

Sections II – IV are partly repeated after Ref. [3]; they present the QSS model used in this paper (Sec. II), the null geodesic equations and properties of redshift along them (Sec. III) and the definition of the extremum redshift surface (ERS, Sec. IV).

In Sec. V, the configuration of the QSS regions is presented, and the time-dependent deflection of light rays

in them is demonstrated on a numerical example. In Sec. VI the rate of angular drift of the deflected rays is calculated. In Sec. VII it is shown by explicit numerical calculation that in the configuration of Sec. V the present observer who registered a gamma-radiation flash at time t_o will no longer see it after 10 minutes. Instead, the radiation coming from the same direction a short while later will have its frequency in the ultraviolet range. (The 10 minutes were chosen as an exemplary duration of an observed GRB [4], but the gamma-ray flash is, in this model, instantaneous; see Sec. IX.)

In Sec. VIII it is shown that the brief duration of the gamma-ray flash is preserved if the initial point and direction of the later-arriving ray are slightly perturbed. Thus, the result of Sec. VII is not overly sensitive to numerical inaccuracies. Section IX is a summary of the results and of the problems that remain to be solved. The appendices present some details of the computations.

II. THE QUASISPHERICAL SZEKERES (QSS) SPACETIME USED IN THIS PAPER

The signature and labelling of coordinates will be $(+, -, -, -)$ and $(x^0, x^1, x^2, x^3) = (t, r, x, y)$ or $(t, r, \vartheta, \varphi)$.

The metric of the QSS spacetimes is [5–7, 13]

$$ds^2 = dt^2 - \frac{(\Phi_{,r} - \Phi \mathcal{E}_{,r} / \mathcal{E})^2}{1 + 2E(r)} dr^2 - \left(\frac{\Phi}{\mathcal{E}}\right)^2 (dx^2 + dy^2),$$
(2.1)

where

$$\mathcal{E} \stackrel{\text{def}}{=} \frac{S}{2} \left[\left(\frac{x - P}{S}\right)^2 + \left(\frac{y - Q}{S}\right)^2 + 1 \right],$$
(2.2)

$P(r)$, $Q(r)$, $S(r)$ and $E(r)$ being arbitrary functions such that $S \neq 0$ and $E \geq -1/2$ at all r.

[*]Electronic address: akr@camk.edu.pl

The source in the Einstein equations is dust ($p = 0$) with the velocity field $u^\alpha = \delta_0{}^\alpha$. The surfaces of constant t and r are nonconcentric spheres, and (x, y) are the stereographic coordinates on each sphere. At a fixed r, they are related to the spherical coordinates by

$$x = P + S \cot(\vartheta/2) \cos\varphi,$$
$$y = Q + S \cot(\vartheta/2) \sin\varphi. \qquad (2.3)$$

The functions (P, Q, S) determine the centres of the spheres in the spaces of constant t (see illustrations in Ref. [2]). Because of the non-concentricity, the QSS spacetimes in general have no symmetry [14].

With $\Lambda = 0$ assumed, $\Phi(t, r)$ obeys

$$\Phi_{,t}{}^2 = 2E(r) + \frac{2M(r)}{\Phi}, \qquad (2.4)$$

where $M(r)$ is an arbitrary function. We will consider only models with $E > 0$, then the solution of (2.4) is

$$\Phi(t, r) = \frac{M}{2E}(\cosh\eta - 1),$$
$$\sinh\eta - \eta = \frac{(2E)^{3/2}}{M}[t - t_B(r)], \qquad (2.5)$$

where $t_B(r)$ is an arbitrary function; $t = t_B(r)$ is the time of the BB singularity, at which $\Phi(t_B, r) = 0$. We assume $\Phi_{,t} > 0$ (the Universe is expanding).

The mass density implied by (2.1) is

$$\kappa\rho = \frac{2(M_{,r} - 3M\mathcal{E}_{,r}/\mathcal{E})}{\Phi^2(\Phi_{,r} - \Phi\mathcal{E}_{,r}/\mathcal{E})}, \qquad \kappa \overset{\text{def}}{=} \frac{8\pi G}{c^2}. \qquad (2.6)$$

This is a mass-dipole superposed on a spherical monopole [15], [6]. The dipole vanishes where $\mathcal{E}_{,r} = 0$. The density is minimum where $\mathcal{E}_{,r}/\mathcal{E}$ is maximum and vice versa [16].

The arbitrary functions must be such that no singularities exist after the BB. This is ensured by [16]:

$$\frac{M_{,r}}{3M} \geq \frac{\mathcal{P}}{S}, \qquad \frac{E_{,r}}{2E} > \frac{\mathcal{P}}{S} \qquad \forall\, r, \qquad (2.7)$$
$$\text{where} \quad \mathcal{P} \overset{\text{def}}{=} \sqrt{(S_{,r})^2 + (P_{,r})^2 + (Q_{,r})^2}. \qquad (2.8)$$

These inequalities imply [16]

$$\frac{M_{,r}}{3M} \geq \frac{\mathcal{E}_{,r}}{\mathcal{E}}, \qquad \frac{E_{,r}}{2E} > \frac{\mathcal{E}_{,r}}{\mathcal{E}} \qquad \forall\, r. \qquad (2.9)$$

The extrema of $\mathcal{E}_{,r}/\mathcal{E}$ with respect to (x, y) are [16]

$$\left.\frac{\mathcal{E}_{,r}}{\mathcal{E}}\right|_{\text{ex}} = \varepsilon_2 \frac{\mathcal{P}}{S}, \qquad \varepsilon_2 = \pm 1, \qquad (2.10)$$

with $+$ at a maximum and $-$ at a minimum; they occur at

$$x = P + \frac{SP_{,r}}{\mathcal{P} + \varepsilon_2 S}, \qquad y = Q + \frac{SQ_{,r}}{\mathcal{P} + \varepsilon_2 S}. \qquad (2.11)$$

The Lemaître [17] – Tolman [18] (L–T) models are contained in (2.1) – (2.2) as the limit of constant (P, Q, S).

The Friedmann limit is obtained from QSS when $E/M^{2/3}$ and t_B are constant (then (P, Q, S) can be made constant by a coordinate transformation). QSS and Friedmann spacetimes can be matched at any constant r.

Because of $p = 0$, the QSS models can describe the evolution of the Universe no further back in time than to the last scattering hypersurface (LSH); see Sec. V.

We will consider such QSS spacetimes whose L–T limit is Model 2 of Ref. [1]. The r-coordinate is chosen so that

$$M = M_0 r^3, \qquad (2.12)$$

and $M_0 = 1$ (kept in formulae for dimensional clarity) [19]. The function $E(r)$, assumed in the form

$$2E/r^2 \overset{\text{def}}{=} -k = 0.4, \qquad (2.13)$$

is the same as in the background Friedmann model.

The units used in numerical calculations were introduced and justified in Ref. [20]. Taking [21]

$$1\ \text{pc} = 3.086 \times 10^{13}\ \text{km}, \quad 1\ \text{y} = 3.156 \times 10^7\ \text{s}, \qquad (2.14)$$

the numerical length unit (NLU) and the numerical time unit (NTU) are defined as follows:

$$1\ \text{NTU} = 1\ \text{NLU} = 9.8 \times 10^{10}\ \text{y} = 3 \times 10^4\ \text{Mpc}. \qquad (2.15)$$
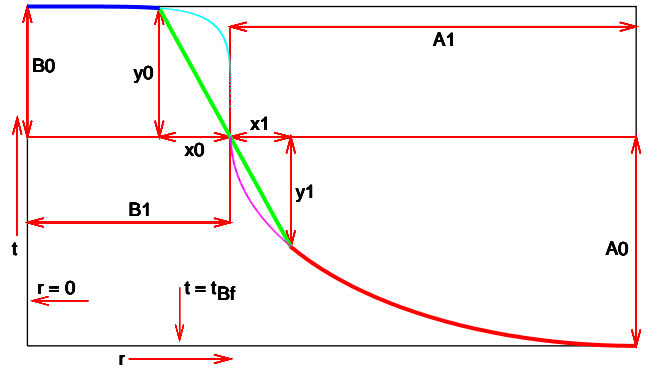

FIG. 1: Parameters of the bang-time profile in the quasi-spherical Szekeres region; see text for explanation.

The BB profile is the same as in Ref. [1], see Fig. 1. It consists of two curved arcs and of a straight line segment joining them. The upper-left arc is a segment of the curve

$$\frac{r^6}{B_1{}^6} + \frac{(t - t_{\text{Bf}} - A_0)^6}{B_0{}^6} = 1, \qquad (2.16)$$

where

$$t_{\text{Bf}} = -0.13945554689046649\ \text{NTU} \approx -13.67 \times 10^9\ \text{years}. \qquad (2.17)$$

The t_{Bf} is the asymptotic value of $t_B(r)$ in the L–T model that mimicked accelerating expansion [19, 20]. This differs by $\sim 1.6\%$ from $(-T)$, where T is the age of the Universe determined by the Planck satellite [22]

$$T = 13.819 \times 10^9\ \text{y} = 0.141\ \text{NTU}. \qquad (2.18)$$

The lower-right arc is a segment of the ellipse[1]

$$\frac{(r - B_1 - A_1)^2}{A_1^2} + \frac{(t - t_{\mathrm{Bf}} - A_0)^2}{A_0^2} = 1. \qquad (2.19)$$

The straight segment passes through the point where the full curves would meet; its slope is determined by x_0.

The free parameters are A_0, A_1, B_0, B_1 and x_0. In Fig. 1 the values of x_0 and A_1 are greatly exaggerated to improve readability. The actual values are [3]

$$\begin{pmatrix} A_0 \\ B_0 \\ A_1 \\ B_1 \\ x_0 \end{pmatrix} = \begin{pmatrix} 0.000026 \text{ NTU} \\ 0.000091 \text{ NTU} \\ 1 \times 10^{-10} \\ 0.015 \\ 10^{-11} \end{pmatrix}, \qquad (2.20)$$

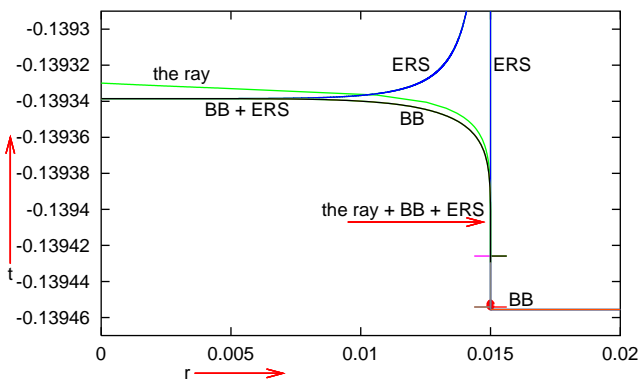and this BB profile is shown[2] in Fig. 2.

FIG. 2: The real BB profile. The horizontal strokes are at the ends of the straight segment. The lower arc from Fig. 1 looks like a short vertical straight line. "The ray" is one with the smallest $1 + z$; it intersects the last scattering hypersurface at the dot. ERS is the extremum redshift surface, see Sec. IV.

The QSS model is axially symmetric, with $P(r) = Q(r) = 0$ and

$$S(r) = \sqrt{a^2 + r^2} \qquad (2.21)$$

(the same as in Ref. [3]), where $a^2 = 0.001$. This $S(r)$ obeys (2.7), which, using (2.12) – (2.13), reduces to

$$1/r > S_{,r}/S. \qquad (2.22)$$

The axis of symmetry is at $x = y = 0$. At $r > r_F$, where

$$r_F = A_1 + B_1, \qquad (2.23)$$

---

[1] In further figures it looks like a vertical straight line segment because A_1 is extremely small.
[2] Figure 2 here is different from Fig. 2 in Ref. [3] – the latter showed an intermediate profile before final optimization.

the BB profile becomes horizontal straight, and the geometry of the model becomes Friedmannian. See Sec. III for remarks on the choice of coordinates in that region.

The Friedmann background is defined by

$$\mathrm{d}s^2 = \mathrm{d}t^2 - \mathcal{R}^2(t) \left[\frac{\mathrm{d}r^2}{1 - kr^2} + r^2 \left(\mathrm{d}\vartheta^2 + \sin^2\vartheta \mathrm{d}\varphi^2 \right) \right],$$
$$(2.24)$$

where k and t_{Bf} are given by (2.13) and (2.17), and

$$\Lambda = 0 \qquad (2.25)$$

is assumed; $t = 0$ is the present time, t_{Bf} is the BB time. The scale factor $\mathcal{R}(t)$ is determined by (2.5) with $\Phi = r\mathcal{R}(t)$, (2.12) – (2.13) and $t_B(r) = t_{\mathrm{Bf}} = $ constant.

The mass-density at the last scattering time in the now-standard ΛCDM model is [1]

$$\kappa\rho_{\mathrm{LS}} = 56.1294161975316 \times 10^9 \text{ (NLU)}^{-2}. \qquad (2.26)$$

In the L–T and Szekeres models it is assumed that a light ray intersects the LSH when the density calculated along it becomes equal to the ρ_{LS} in (2.26).

With (2.24), (2.25), (2.13) and (2.17), the ρ_{LS} of (2.26) occurs at the redshift relative to the present time

$$1 + z_{\mathrm{LS}}^b = 952.611615159. \qquad (2.27)$$

This differs by $\sim 12.7\%$ from the ΛCDM value $z_{\mathrm{LS}} = 1090$ [22, 23]. To bring our model to agreement with this, laborious re-calculations would be required. Since the model needs improvements anyway, we will rather stick to (2.25), (2.13) and (2.17), to be able to compare the present results with the earlier ones.

III. NULL GEODESICS IN THE AXIALLY SYMMETRIC QSS SPACETIMES

In (2.1) – (2.2) $x = \infty$ and $y = \infty$ are at the pole of the stereographic projection of a sphere. This is a coordinate singularity where numerical integration of geodesics breaks down. So, we introduce the coordinates (ϑ, φ) by

$$x = S_F \cot(\vartheta/2) \cos\varphi, \qquad y = S_F \cot(\vartheta/2) \sin\varphi, \quad (3.1)$$

where

$$S_F \stackrel{\text{def}}{=} S(r_F) = \sqrt{a^2 + r_F^2} \qquad (3.2)$$

is the value of S at the Szekeres/Friedmann boundary. This changes (2.1) and (2.2) to

$$\mathrm{d}s^2 = \mathrm{d}t^2 - \frac{\mathcal{N}^2 \mathrm{d}r^2}{1 + 2E(r)} - \left(\frac{\Phi}{\mathcal{F}} \right)^2 \left(\mathrm{d}\vartheta^2 + \sin^2\vartheta \mathrm{d}\varphi^2 \right),$$
$$(3.3)$$

$$\mathcal{F} = \frac{S_F}{2S} \left(1 + \cos\vartheta \right) + \frac{S}{2S_F} \left(1 - \cos\vartheta \right), \qquad (3.4)$$

where

$$\mathcal{N} \stackrel{\text{def}}{=} \Phi_{,r} - \Phi \mathcal{F}_{,r} / \mathcal{F}. \qquad (3.5)$$

In general, (ϑ, φ) are *not* the spherical polar coordinates because $\mathcal{F}$ depends on ϑ. The dipole equator $\mathcal{F}_{,r} = 0$ is at $\cot(\vartheta_{\text{eq}}/2) = S/S_F$ (so $\vartheta_{\text{eq}} = \pi/2$ in the Friedmann region including the QSS boundary, see further in this section). At $r = r_F$ we have $\mathcal{F} = 1$ and (ϑ, φ) become the spherical coordinates with the origin at $r = 0$.

Along a geodesic we denote

$$\left(k^t, k^r, k^\vartheta, k^\varphi \right) \stackrel{\text{def}}{=} \frac{\mathrm{d}(t, r, \vartheta, \varphi)}{\mathrm{d}\lambda}, \qquad (3.6)$$

where λ is an affine parameter. In the (ϑ, φ) coordinates, the geodesic equations for (3.3) – (3.4) are

$$\frac{\mathrm{d}k^t}{\mathrm{d}\lambda} + \frac{\mathcal{N}\mathcal{N}_{,t}}{1 + 2E} \left(k^r \right)^2 + \frac{\Phi \Phi_{,t}}{\mathcal{F}^2} \left[\left(k^\vartheta \right)^2 + \sin^2 \vartheta \left(k^\varphi \right)^2 \right] = 0, \qquad (3.7)$$

$$\frac{\mathrm{d}k^r}{\mathrm{d}\lambda} + 2 \frac{\mathcal{N}_{,t}}{\mathcal{N}} k^t k^r$$
$$+ \left(\frac{\mathcal{N}_{,r}}{\mathcal{N}} - \frac{E_{,r}}{1 + 2E} \right) \left(k^r \right)^2 + 2 \frac{S_{,r} \sin \vartheta \Phi}{S \mathcal{F}^2 \mathcal{N}} k^r k^\vartheta$$
$$- \frac{\Phi(1 + 2E)}{\mathcal{F}^2 \mathcal{N}} \left[\left(k^\vartheta \right)^2 + \sin^2 \vartheta \left(k^\varphi \right)^2 \right] = 0, \quad (3.8)$$

$$\frac{\mathrm{d}k^\vartheta}{\mathrm{d}\lambda} + 2 \frac{\Phi_{,t}}{\Phi} k^t k^\vartheta - \frac{S_{,r} \sin \vartheta \mathcal{N}}{S \Phi(1 + 2E)} \left(k^r \right)^2 + 2 \frac{\mathcal{N}}{\Phi} k^r k^\vartheta$$
$$+ \frac{\mathcal{F}_{,\vartheta}}{\mathcal{F}} \left[-\left(k^\vartheta \right)^2 + \sin^2 \vartheta \left(k^\varphi \right)^2 \right]$$
$$- \cos \vartheta \sin \vartheta \left(k^\varphi \right)^2 = 0, \qquad (3.9)$$

$$\frac{\mathrm{d}k^\varphi}{\mathrm{d}\lambda} + 2 \frac{\Phi_{,t}}{\Phi} k^t k^\varphi + 2 \frac{\mathcal{N}}{\Phi} k^r k^\varphi$$
$$+ 2 \left[\frac{\cos \vartheta}{\sin \vartheta} - \frac{\mathcal{F}_{,\vartheta}}{\mathcal{F}} \right] k^\vartheta k^\varphi = 0. \qquad (3.10)$$

The geodesics determined by (3.7) – (3.10) are null when

$$\left(k^t \right)^2 - \frac{\mathcal{N}^2 \left(k^r \right)^2}{1 + 2E(r)} - \left(\frac{\Phi}{\mathcal{F}} \right)^2 \left[\left(k^\vartheta \right)^2 + \sin^2 \vartheta \left(k^\varphi \right)^2 \right] = 0. \qquad (3.11)$$

On past-directed rays $k^t < 0$, and λ along each of them can be chosen such that at the observation point

$$k_o^t = -1. \qquad (3.12)$$

(On future-directed rays $k^t > 0$ and a convenient choice of λ is $k_e^t = +1$.)

For correspondence with Ref. [1], in the Friedmann region we choose the coordinates so that

$$S = \sqrt{a^2 + r_F^2} = S_F. \qquad (3.13)$$

Then, throughout the Friedmann region, $\mathcal{F} = 1$ and (ϑ, φ) are the spherical coordinates. They coincide with the coordinates of the QSS region at $r = r_F$.

To calculate k^r on nonradial rays, (3.11) will be used, which is insensitive to the sign of k^r. This sign will be changed at each point where k^r reaches zero by the numerical program integrating $\{(3.7), (3.9) - (3.11)\}$.

Note that $\vartheta \equiv 0$ and $\vartheta \equiv \pi$ are solutions of (3.9). These rays intersect every space of constant t on the symmetry axis; they are called axial rays. As follows from (3.9), there exist no null geodesics on which $k^\varphi \equiv 0$ and ϑ has any constant value other than 0 or π (because with $0 \neq \vartheta \neq \pi$, $k^\varphi \equiv 0$ and $k^\vartheta = 0$ at a point, Eq. (3.9) implies $\mathrm{d}k^\vartheta/\mathrm{d}\lambda \neq 0$). Consequently, in the axially symmetric case the only analogues of radial directions are $\vartheta = 0$ and $\vartheta = \pi$; along these geodesics φ is undetermined.

Along a ray emitted at P_e and observed at P_o, with k^α being affinely parametrised, we have

$$1 + z = \frac{(u_\alpha k^\alpha)_e}{(u_\alpha k^\alpha)_o}, \qquad (3.14)$$

where u_α are four-velocities of the emitter and of the observer [24]. In our case, both the emitter and the observer comove with the cosmic matter, so $u_\alpha = \delta^0{}_\alpha$, and the affine parameter is chosen so that (3.12) holds; then

$$1 + z = -k_e{}^t. \qquad (3.15)$$

Equation (3.10) has the first integral:

$$k^\varphi \sin^2 \vartheta \Phi^2 / \mathcal{F}^2 = J_0, \qquad (3.16)$$

where J_0 is constant along each geodesic. When (3.16) is substituted in (3.11), the following results:

$$(k^t)^2 = \frac{\mathcal{N}^2 \left(k^r \right)^2}{1 + 2E} + \left(\frac{\Phi}{\mathcal{F}} \right)^2 \left(k^\vartheta \right)^2 + \left(\frac{J_0 \mathcal{F}}{\sin \vartheta \Phi} \right)^2. \qquad (3.17)$$

At the observation/emission point, (3.12)/(3.15), respectively, apply. Equations (3.17) and (3.15) show that for rays emitted at the BB, where $\Phi = 0$, the observed redshift is infinite when $J_0 \neq 0$. A necessary condition for infinite blueshift $(1 + z_o = 0)$ is thus $J_0 = 0$, so

(a) either $k^\varphi = 0$,

(b) or $\vartheta = 0, \pi$ along the ray (note that (3.16) implies $J_0 / \sin \vartheta \to 0$ when $\vartheta \to 0, \pi$).

Condition (b) appears to be also sufficient, but so far this has been demonstrated only numerically in concrete examples of QSS models ([2, 3]).

Condition (a) is *not* sufficient, and Ref. [2] contains numerical counterexamples: there exist rays that proceed in a surface of constant φ, but approach the BB with $z \to \infty$; the value of ϑ along them changes and is different from $0, \pi$. For those rays, (3.17) with the last term being zero implies one more thing

$$\text{If } \lim_{t \to t_B} z = \infty \text{ and } \lim_{t \to t_B} |k^r| < \infty$$
$$\text{then } \lim_{t \to t_B} k^\vartheta = \pm \infty, \qquad (3.18)$$

i.e., such rays approach the BB tangentially to the surfaces of constant r. Examples will appear in Sec. VI.

Consider a ray proceeding from event P_1 to P_2 and then from P_2 to P_3. Denote the redshifts acquired in the intervals $[P_1, P_2]$, $[P_2, P_3]$ and $[P_1, P_3] = [P_1, P_2] \cup [P_2, P_3]$ by z_{12}, z_{23} and z_{13}, respectively. Then, from (3.14),

$$1 + z_{13} = (1 + z_{12})(1 + z_{23}). \qquad (3.19)$$

Thus, for a ray proceeding to the past from P_1 to P_2, and then back to the future from P_2 to P_1:

$$1 + z_{12} = \frac{1}{1 + z_{21}}. \qquad (3.20)$$

IV. THE EXTREMUM REDSHIFT SURFACE

Let a null geodesic stay in the surface $\{\vartheta, \varphi\} = \{\pi, \text{constant}\}$. Then $k^r \neq 0$ at all its points, see (3.11). Assume it is past-directed and has its initial point at $r = 0$. Thus, r has to increase along it and can be used as a parameter. Using (3.15), we then obtain from (3.7)

$$\frac{dz}{dr} = \frac{\mathcal{N}\mathcal{N},_t}{1 + 2E}\, k^r. \qquad (4.1)$$

Since $\mathcal{N} \neq 0$ from no-shell-crossing conditions [16] and $k^r > 0$, the extrema of z on such a geodesic occur where

$$\mathcal{N},_t \equiv \Phi,_{tr} - \Phi,_t\, \mathcal{F},_r /\mathcal{F} = 0. \qquad (4.2)$$

Since $\vartheta = \pi$ was assumed, the set defined by (4.2) is 2-dimensional; it is the Extremum Redshift Surface (ERS) [2]. Equation (4.2) is equivalent to [2]

$$\chi^4 + \chi^3 = -k^3 \left[\frac{r t_{B,r}}{4 M_0 (1 - r S,_r /S)} \right]^2, \qquad (4.3)$$

where

$$\chi \overset{\text{def}}{=} \sinh^2(\eta/2) \qquad (4.4)$$

With $k < 0$, (4.3) is solvable for χ at any r, since its left-hand side is independent of r, monotonic in χ and varies from 0 to $+\infty$, while the right-hand side is non-negative. The right half of the ERS profile with the parameters of (2.20) is shown in Fig. 2.

In the limit $S,_r \to 0$ (which occurs at $a \to \infty$), (4.3) reproduces the equation of the Extremum Redshift *Hypersurface* (ERH) of Ref. [1].

Equation (4.3) was derived for null geodesics proceeding along $\vartheta = \pi$, where the mass dipole is maximum, $\mathcal{F},_r /\mathcal{F} = S,_r /S > 0$. With S given by (2.21) we have

$$F_1 \overset{\text{def}}{=} 1/(1 - r S,_r /S) = (r/a)^2 + 1 > 1, \qquad (4.5)$$

so, at a given r, the ERS has a greater η (greater $t - t_B$) than the ERH of the corresponding L–T model. Moreover, the χ of (4.3) is greater when a is smaller.

Conversely, for a ray proceeding along the dipole minimum (where $\vartheta = 0$), the factor F_1 is replaced by

$$F_2 \overset{\text{def}}{=} 1/(1 + r S,_r /S) = \frac{a^2 + r^2}{a^2 + 2r^2} < 1, \qquad (4.6)$$

and so the ERS has a *smaller* $t - t_B$ than the ERH in L–T. Also here, a smaller a has a more pronounced effect.

Extrema of redshift exist along other directions than $\vartheta = 0$ and $\vartheta = \pi$ (see examples in Sec. VII), but a general equation defining their loci remains to be derived.

V. THE TIME-DEPENDENT DEFLECTION OF LIGHT RAYS

From here on we will consider only the rays proceeding within the surface of constant φ.

For the source of the gamma rays we take the BB hump of Fig. 3. We assume that the maximally blueshifted axial ray emitted there (at the big dot in Fig. 2 and near to the tip of the arrow in the QSS1 circle in Fig. 3) passes, on its way to the observer, through another axially symmetric QSS region (QSS2 in Fig. 3), where it is deflected. The parameters of QSS2 are assumed the same as in QSS1. In general, the angle of deflection changes with time in consequence of the cosmic drift [10, 12]. Consequently, if the maximally blueshifted ray hits a given observer at a given time, an axial ray emitted a while later will miss the observer, apart from a few exceptional cases (see below). After a short while, the rays seen by the observer in the same direction will be coming from other regions of the same source and will be less blueshifted, i.e., they will form the afterglow. See Sec. VI for a more detailed description.

A ray that hits QSS2 along the symmetry axis (from either the dipole maximum or minimum side) is not deflected [10]. But the directions in the dipole equator plane, $\vartheta = \pi/2$, are also special. If a ray hits QSS2 there having proceeded along $\vartheta = \pi/2$ in the Friedmann region, then a deflection will occur, but there will be no drift.[3] For rays that hit QSS2 from other directions, the time-dependent deflection is to be expected.

In the following, we will use two coordinate charts of the class (3.3) – (3.5), one centered at the origin of QSS1, and the other centered at the origin of QSS2. Their t will be the same, but the r-coordinates will differ. Whenever confusion may arise, we will denote the r of QSS1 by r_{S1}, and the other one by r_{S2}.

We consider a ray that was emitted from the LSH at the symmetry axis of QSS1 on the dipole maximum side, and proceeds along this axis. The initial point is the one that gives the maximally strong blueshift. (It is "ray A" in Sec. 9 of Ref. [3] and "the ray" shown in Fig. 2). The ray then passes all through QSS1 and emerges into the Friedmann region (after passing the origin of QSS1 it becomes "ray B" of Ref. [3]). This part of the ray's path is not shown in Fig. 3; in the following it will be called the Upray. On it, we choose the point just behind

————

[3] This effect was verified numerically; its reason is not evident in the geodesic equations.
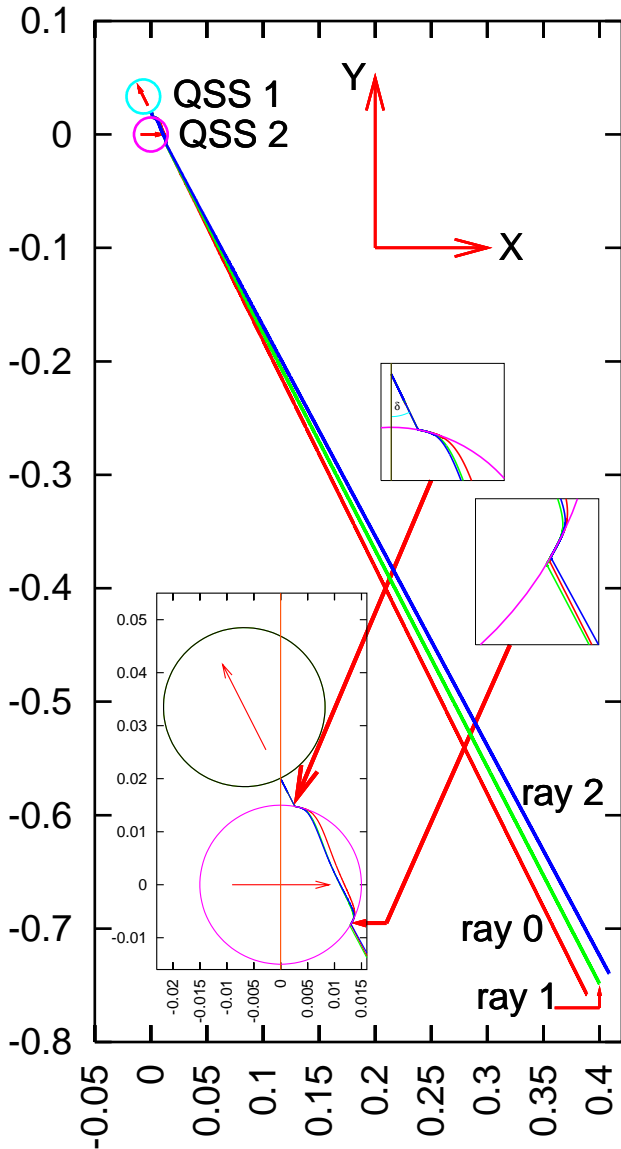
FIG. 3: Projection of Rays 0, 1 and 2 on a surface of constant t and φ. The coordinates are related to those of (3.3) – (3.4) by $X = -r\cos\vartheta, Y = r\sin\vartheta$ (ϑ increases clockwise). QSS1 is the Szekeres region that generates the blueshift, QSS2 deflects the rays. The arrows inside circles mark the directions of mass dipole maxima. The rays end at the present time, $t = 0$. The insets show the neighbourhoods of the entry and exit points of the rays to the QSS2 region. More explanation in the text.

the QSS1 region, with

$$(r_{S1}, t) = (r, t)_1 = \qquad\qquad (5.1)$$
$$(0.0150907023847052114, -0.13926900571845113),$$
$$z_1 = -0.39590497158301252 \qquad (5.2)$$

(these numbers are taken from the numerical tables for ray B [3]). We take (t_1, z_1) as the initial data for Ray 0. (Note: z_1 is the *upward* redshift between $r_{S1} = 0$ and $r_{S1} = r_1$. The true (downward) redshift between these points is $1 + z_{1\ \text{true}} = 1/(1 + z_1)$.)

For the initial r_{S2} on Ray 0 we take

$$r_{S2} = r_i = 0.02. \qquad (5.3)$$

We assume that the dipole maximum of QSS2 lies on $\vartheta = \pi$ in Fig. 3, while the angle between the direction of the ray at (t_1, r_i) and the dipole equator of QSS2 is

$$\delta = \arctan(1/2); \qquad (5.4)$$

see the uppermost inset in Fig. 3. The values of r_i and δ were chosen such that the drift is clearly visible in the illustrations, while the two QSS regions are not too close to each other. The angle of deflection becomes larger when r_i is smaller and vice versa. The angle δ is related to the initial k^ϑ by

$$\sin\delta = \frac{k_i^\vartheta \Phi(t_i, r_i)}{1 + z_1} \qquad (5.5)$$

(see derivation in Appendix A), with $\Phi(t_i, r_i)$ calculated from (2.5) using (2.12) and (2.13), and (2.17) for t_B.

The upward redshift to $t = 0$ on Ray 0 is[4]

$$(1 + z)_{3\ \text{up}} = 7.19256480334251602 \times 10^{-3}. \qquad (5.6)$$

The z_1 in (5.2) is the upward z between $r_{S1} = 0$ and $r_{S1} = r_1$. Consequently, (5.6) is the upward z between $r_{S1} = 0$ and the present observer. The proper z between the LSH and $r_{S1} = 0$ was calculated in Ref. [3]:

$$1 + z_{\text{ols3}} = 1.11939135405414447 \times 10^{-7}. \qquad (5.7)$$

So, the proper $1 + z$ between the last scattering in QSS1 and the present time is

$$1 + z_3 = \frac{1 + z_{\text{ols3}}}{1 + z_{3\ \text{up}}} = 1.55631737031266357 \times 10^{-5}. \qquad (5.8)$$

This is near to 1.553×10^{-5} of Ref. [3]; the difference arose because in Ref. [3] the intervening QSS2 region was absent. The $1 + z_3$ of (5.8) is within the range $1 + z < 1.689 \times 10^{-5}$ needed to blueshift the emission frequencies of hydrogen into the gamma sector [1].

Ray 0 overshot the present time $t = 0$ in consequence of numerical errors. The calculation stopped at

$$t_{\text{fin}} = 1.29738987343870121 \times 10^{-10}\ \text{NTU}, \qquad (5.9)$$

and the other coordinates of the endpoint were

$$(r_{S2}, \vartheta) = (r, \vartheta)_{\text{fin}} = \qquad\qquad (5.10)$$
$$(0.85217686701400219,\ 4.2386753628314251)$$

(recall: ϑ is counted from the $X < 0$ direction clockwise).

---

[4] For reproducibility of the results, the numbers are quoted up to 17 decimal digits. Such precision was needed to capture time differences of ≈ 10 min at the observer – see Secs. VI – VII.

Rays 1 and 2 have their initial points at the same $r_{S2} = r_i = 0.02$ as Ray 0, and the initial direction still determined by δ of (5.4), but the initial t later by 0.00002 NTU (Ray 1) and 0.00004 NTU (Ray 2). The angle δ being the same means that the initial directions are parallel-transported along the world line of the emitter; see Appendix B for more on this.

As seen in Fig. 3, each ray is deflected by a different angle when passing through QSS2. This is the cosmic drift (non-repeatability of light paths) of Refs. [10–12]. On comparing the two upper insets in Fig. 3 one sees that the projections of Rays 0 and 2 intersect at the edge of QSS2: Ray 0 goes further than Ray 2 around the BB hump. Similarly, the projections of Ray 0 and Ray 1 intersect at point P of coordinates $(X, Y) \approx (0.019987, -0.02143)$.
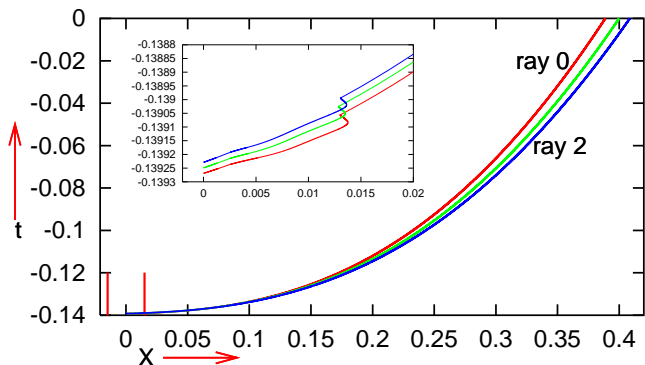
FIG. 4: Projection of rays 0 – 2 on the $Y = 0$ coordinate plane. The vertical strokes show the borders of QSS2. The inset shows the segments of the rays inside and near QSS2.
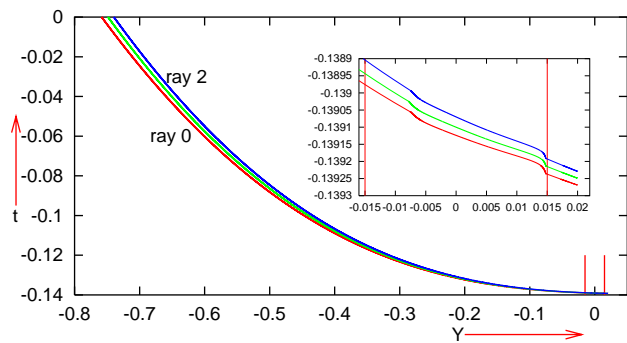

FIG. 5: Projection of rays 0 – 2 on the $X = 0$ coordinate plane. The vertical strokes show the borders of QSS2. The inset shows the segments of the rays inside and near QSS2.

Although the projections of Rays 0 and 1 on the (X, Y)-surface intersect at P, the rays do not intersect in spacetime, as is seen from their projections on the (X, t) and (Y, t) coordinate surfaces in Figs. 4 and 5, respectively. The intersecting (X, Y)-projections imply that an observer at P would register both Ray 0 and (suitably later, from a different direction) Ray 1.

Figures 6 and 7 show $[1 + z(r)] \times 10^5$ along Ray 0. In short segments near the borders of QSS2, $1 + z$ decreases when followed along the ray to the future. However, the times of flight of the rays through QSS2 are made longer by the deflections. The net result is that the ray spends more time in the redshift-generating region, and the final $1 + z$ is larger than it would be in the absence of QSS2 – see (5.8) and the remark under it.
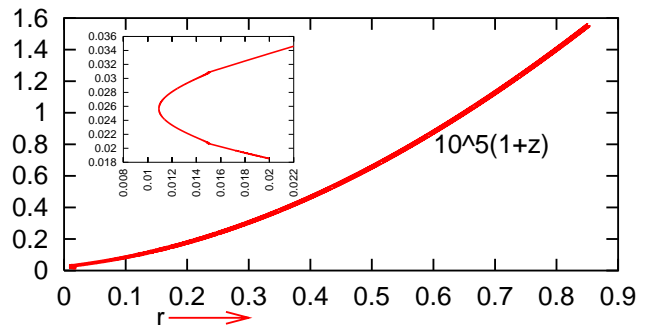

FIG. 6: **Main panel:** The graph of $[1 + z(r)] \times 10^5$ along Ray 0. **Inset:** The segment of the graph where the local extrema of $z(r)$ are present; they are displayed in Fig. 7.
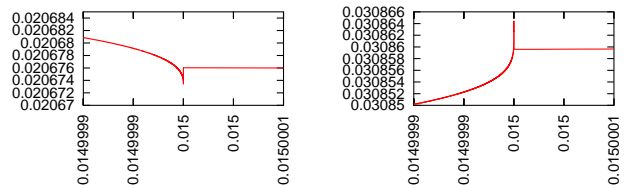

FIG. 7: Closeup views on the curve from Fig. 6 around the points where it crosses the edges of QSS2.

VI. RATE OF ANGULAR DRIFT OF THE RAYS

Now we calculate the average rate of the angular drift of the rays applying a few approximations. As the first approximation, we take the angles between the images of the future-end segments of the rays in Fig. 3 for the real angles in spacetime. Since these angles are small, the departure from the exact result should be tolerable. As shown in Appendix C, the angle between the end segments of Rays 2 and 0 is

$$\Delta\beta = 1.79491638375138503°. \tag{6.1}$$

The time difference between rays 0 and 2 at their initial points at $r_{S2} = r_i$ is, from (2.14) and (2.15),

$$\Delta t = 0.00004 \text{ NTU} = 39.2 \times 10^5 \text{ y}$$
$$= 2.06192 \times 10^{12} \text{ min.} \tag{6.2}$$

This implies the average rate of angular drift, with respect to the source time

$$\frac{d\beta}{dt} = 4.57886832589639038 \times 10^{-7} \ °/y$$
$$= 8.70507286292089426 \times 10^{-13} \ °/\text{min}$$
$$= 0.15193218308397861 \times 10^{-13} \ \text{rad/min.} \quad (6.3)$$

In (6.3), the time is counted between the initial points of Rays 0 and 2, at $(r, \vartheta)_{S2} = (r_i, \pi/2)$, with r_i given by (5.3). The upward redshift on Ray 0 from $r_{S1} = 0$ to the present time is the $z_{3 \ \text{up}}$ given by (5.6). Hence, the proper redshift on Ray 0 between $r_{S2} = r_i$ and the present time is

$$1 + z_{\text{ip}} = \frac{1 + z_1}{1 + z_{3 \ \text{up}}} = 83.98881969561866230, \quad (6.4)$$

where z_1 is given by (5.2). So, the time difference Δt at (r_i, t_1) results in the time difference $(1 + z_{\text{ip}}) \times \Delta t$ at the observer. The rate of angular drift at the observer is thus

$$\left.\frac{d\alpha}{dt}\right|_{\text{observer}} = \frac{d\beta}{dt} \Big/ (1 + z_{\text{ip}})$$
$$= 1.80895723543432844 \times 10^{-16} \ \text{rad/min.} \quad (6.5)$$

As a curiosity, in Ref. [10] (an off-center observer in a spherical void, observing galaxies around her) the cosmic drift was $\leq 10^{-6}$ arcsec/y $\approx 9.22 \times 10^{-18}$ rad/min, i.e. ≈ 19.6 times smaller than (6.5).

The observed GRBs typically last from less than a second to a few minutes [4]. Let 10 minutes be the reference time. Imagine a ray in our model reaching the observer 10 minutes later than Ray 0 from the same direction. Will it still be a gamma ray?

A direct answer would require emitting a ray from the observer position back in time later by

$$\tau = 10 \ \text{min} = 1.93993947388841468 \times 10^{-16} \ \text{NTU} \quad (6.6)$$

(from (2.14) – (2.15)) than the t_{fin} of (5.9), in the direction opposite to Ray 0. But a ray having its initial point so close to the endpoint of Ray 0 could be numerically distinguishable from Ray 0 only at very high precision that is inaccessible to this author.[5] Therefore, we shall again resort to an approximate estimate.

Ray 2 was sent from its initial point later by 0.00004 NTU than Ray 0. This translates, by (6.4), to

$$\Delta t_2 \approx 0.00335955278782475 \ \text{NTU} \quad (6.7)$$

at the present time, $t = 0$. So, we send a ray (call it Backray 0) from the observer position given by (5.9) –

_____

[5] Such a ray would travel through nearly the whole lifetime of the Universe. To capture time differences counted in seconds, the numerical time-step would have to be of the order of 1 s. Using (2.14) and taking 13.819×10^9 y for the age of the Universe [22], the calculation would require $\approx 43 \times 10^{16}$ steps.

(5.10) backward in time, with the initial $t = t_{\text{fin}} + \Delta t_2$, and with the initial direction opposite to the final direction of Ray 0. There were difficulties with assigning the correct number to the initial direction, see Appendix D. The number finally chosen was

$$\mu \overset{\text{def}}{=} k^\vartheta / k^r = 0.0107412585641537794 \quad (6.8)$$

With this value, at the first contact with the edge of QSS2 Backray 0 and Ray 0 coincide to better than 10^{-8} in both X and Y; see Appendix D again (but the coincidence is not as good all the way).
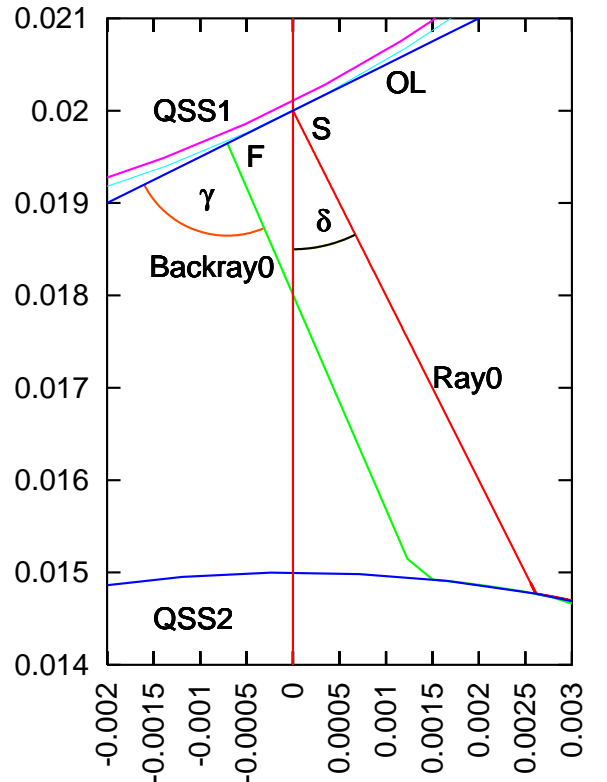

FIG. 8: Projections of Ray 0 and Backray 0 on a surface of constant t in a vicinity of QSS1. The line OL is orthogonal to the projection of Ray 0 at its initial point S; Backray 0 was stopped where its projection crossed OL, at point F in spacetime. The thin arc tangent to OL at S is concentric with QSS1 and has the radius r_1 given by (5.1). The other arcs are borders of the QSS regions.

The integration of Backray 0 was stopped at the 2-surface S_b in spacetime given by the equations

$$r = \frac{r_i}{\sin\vartheta + \tan\delta\cos\vartheta} \equiv \frac{r_i\cos\delta}{\sin(\delta + \vartheta)},$$
$$\varphi = \text{constant.} \quad (6.9)$$

This surface is orthogonal to Ray 0 at its initial point S. It intersects the plane of Fig. 8 along the straight line OL, which has the equation

$$Y = r_i + X\tan\delta, \quad (6.10)$$

where r_i and δ are given by (5.3) – (5.4) and (X, Y) are the coordinates in Fig. 8. The point where Backray 0 hit S_b will be denoted F. Stopping Backray 0 there was convenient for prolonging it into the QSS1 region.[6]

The surface S_b and the line OL are at the same time tangent at S to the circle of radius $r_{S1} = r_1$, where Ray 0 took over from Upray; see Fig. 8.

The following parameters of Backray 0 at F will be needed for further calculations:

$$r_b = 0.0196597503597857326, \quad (6.11)$$
$$t_b = -0.13922666531999014, \quad (6.12)$$
$$\vartheta_b = 1.5348829837350006, \quad (6.13)$$
$$1 + z_b = 74.080313337692317, \quad (6.14)$$
$$\mathcal{R}(t_b) = 0.00617900818769279159. \quad (6.15)$$

Imagine a family of past-directed rays, all emitted from $(r, \vartheta) = (r, \vartheta)_{\text{fin}}$ of (5.10), in the direction opposite to the final direction of Ray 0, with their emission instants continuously increased from $t = t_{\text{fin}}$ of (5.9) to $t_{\text{fin}} + \Delta t_2$ of (6.7). Call this family $\mathcal{G}$ (for "geodesics"). The earliest of these rays is the time-reverse of Ray 0, the last coincides with Backray 0. Their intersections with the surface S_b form an arc connecting point S to point F. The arc SF represents the spatial drift of the endpoint of Backray 0 with respect to the initial point of Ray 0.

The angle γ between the tangent vector to the arc SF at F and the direction vector of Backray 0 at F is

$$\gamma = 1.5137231069990575 \text{ rad}$$
$$= 86.729945382475933° \implies$$
$$\widetilde{\gamma} \overset{\text{def}}{=} \pi/2 - \gamma = 0.0570732197958390142 \text{ rad}$$
$$= 3.2700546175240777°. \quad (6.16)$$

see Appendix E. The (X, Y) coordinates of F are

$$X_b = -r_b \cos\vartheta_b = -7.05895596023793498 \times 10^{-4},$$
$$Y_b = r \sin\vartheta_b = 0.0196470734618825471, \quad (6.17)$$

where r_b and ϑ_b are given by (6.11) and (6.13). The time-coordinates of points S and F in spacetime differ by

$$\Delta t_1 = t_b - t_1 = 4.234039846099 \times 10^{-5} \text{ NTU}. \quad (6.18)$$

Now take a ray of family $\mathcal{G}$ (call it Backray N) that was emitted back in time from $(r, \vartheta)_{\text{fin}}$ by $U\Delta t_2$ later than the t_{fin} of (5.9), where U is small and Δt_2 is given by (6.7). The point of intersection of Backray N with the surface S_b, denoted P_N, lies on the arc SF near to the point S. Quantities referrring to P_N will carry the subscript N. We make two more approximations:

1. The arc SP_N coincides with the straight line segment $S\overline{P_N}$, tangent to SP_N at S, where $\overline{P_N}$ is the projection of P_N on the plane of Fig. 8.

2. The X_N coordinate of P_N, the angle $\widetilde{\gamma}_N$ between Backray N and the normal to the arc SP_N at P_N, the $\Delta t_N \overset{\text{def}}{=} t_N - t_1$ and the redshift difference $z_{\text{ip}} - z_N$ are related to X_b, $\widetilde{\gamma}$, Δt_1 and $z_{\text{ip}} - z_b$ all by the factor U.

It is not obvious how precise these approximations are because, as was seen in Fig. 3, the directions of the rays do not necessarily change uniformly: the projections of some rays intersect. We leave the problem of verifying the correctness of these assumptions (and possible improvements upon them) for the future. The approximation should be better, the shorter $S\overline{P_N}$ is.

We wish to calculate by how much the past endpoint P_N and the direction of Backray N at P_N will differ from those of Ray 0 at S when $U = 10$ minutes/Δt_2, i.e.,

$$U = 5.77439795236701905 \times 10^{-14} \quad (6.19)$$

from (6.6) and (6.7). Then we obtain at P_N

$$X_N \overset{\text{def}}{=} -Ur_b \cos\vartheta_b$$
$$= -4.07612208426468965 \times 10^{-17}, \quad (6.20)$$
$$Y_N \overset{\text{def}}{=} r_i + X_N/\tan\delta = r_i + 2X_N$$
$$= 1.99999999999999185 \times 10^{-2}, \quad (6.21)$$
$$\widetilde{\gamma}_N = U\widetilde{\gamma}$$
$$= 3.29563483524085620 \times 10^{-15} \text{ rad}, (6.22)$$
$$\Delta t_N = U\Delta t_1 \quad (6.23)$$
$$= 2.44490310175544341 \times 10^{-18} \text{ NTU},$$
$$1 + z_N = 1 + z_{\text{ip}} - U(z_{\text{ip}} - z_b)$$
$$= 83.988819695618090. \quad (6.24)$$

From (6.20) – (6.21), the $(r, \vartheta)_{\text{S2}}$ coordinates of P_N are

$$\vartheta_N = \arctan[Y_N/(-X_N)]$$
$$= 1.5707963267948946 \text{ rad}, \quad (6.25)$$
$$r_N = Y_N/\sin\vartheta_N$$
$$= 1.99999999999999185 \times 10^{-2}. \quad (6.26)$$

The program that calculated this does not see the difference between Y_N and r_N. This is because $\pi/2 - \vartheta_N = 2.03806104213235315 \times 10^{-15}$, and the Fortran program finds $\sin\vartheta_N = 1$ up to 16th decimal place. (The difference $\pi/2 - \vartheta_N$ is not to be confused with $\widetilde{\gamma}_N$. The ϑ_N is the value of ϑ_{S2} at the endpoint of Backray N, while $\widetilde{\gamma}_N$ is the angle between the direction of Backray N at the endpoint and the normal to $\overline{\text{SF}}$ there.)

The point $\overline{P_N}$, lying on OL very near to the point S, lies very nearly on the circle of radius $r_{S1} = r_1$ surrounding the QSS1 region. So, we make one more approximation and assume that $\overline{P_N}$ lies on that circle. The error in r committed thereby is smaller than 10^{-17}.

---

[6] The discontinuity in the slope of Backray 0 at the edge of QSS2 in Fig. 8 resulted from interpolation – only 1 in 600 calculated points is used by the drawing program.

VII. ACCOUNTING FOR THE SHORT-LIVEDNESS OF THE GAMMA-RAY FLASH

We now send a new ray (call it Downray 1), backward in time, in prolongation of Backray N. What is the blueshift or redshift on this ray when it crosses the LSH?

The numbers in (6.20) and (6.22) allow us to calculate the initial direction for Downray 1 in terms of the $(r, \vartheta)_{S1}$ coordinates; see the sketch in Fig. 9. It has its initial point at $r_{S1} = r_1$ given by (5.1), shifted by

$$H \stackrel{\text{def}}{=} |X_N| / \cos\delta = \sqrt{5}\,|X_N|\,/2$$
$$= 4.55724303250198597 \times 10^{-17} \quad (7.1)$$

toward $Y_{S1} > 0$ with respect to the symmetry axis. Its initial direction is inclined at the angle $\gamma_N = \pi/2 - \widetilde{\gamma}_N$ to the OL line. The ϑ_{S1} of its initial point is ε given by

$$\tan\varepsilon = H/r_1 = 3.01990120560648060 \times 10^{-15}. \quad (7.2)$$

The Fortran 90 program sees no difference between ε and $\tan\varepsilon$ up to the level of 10^{-17}.
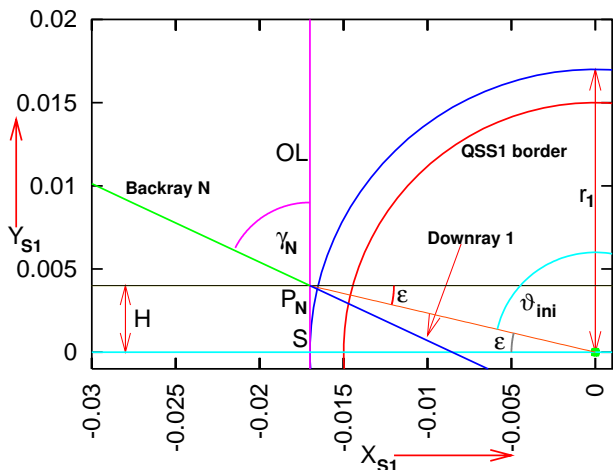

FIG. 9: Sketch of Backray N near its past endpoint and of Downray 1 that continues in the same direction into the QSS1 region. The values of H, r_1, ε and $\pi/2 - \gamma_N = \widetilde{\gamma}_N$ are much exaggerated. The origin of the (X, Y) coordinates in this graph coincides with the origin of QSS1.

The tangent vector to Downray 1 at the point $(t, r, \vartheta) = (t_1 + \Delta t_N, r_1, \varepsilon)$ is

$$k_N^r = \frac{\sqrt{1 - kr_1^2}\,(1 + z_N)}{\mathcal{R}_N \mathcal{D}}$$
$$\times \left(-\tan\varepsilon \sin\widetilde{\gamma}_N - \sqrt{1 - kr_1^2}\cos\widetilde{\gamma}_N\right), \quad (7.3)$$
$$k_N^\vartheta = \frac{1 + z_N}{r_1 \mathcal{R}_N \mathcal{D}}$$
$$\times \left(-\sqrt{1 - kr_1^2}\sin\widetilde{\gamma}_N + \tan\varepsilon\cos\widetilde{\gamma}_N\right), \quad (7.4)$$
$$\mathcal{D} \stackrel{\text{def}}{=} \sqrt{1 - kr_1^2 + \tan^2\varepsilon}, \quad \mathcal{R}_N \stackrel{\text{def}}{=} \mathcal{R}(t_N); \quad (7.5)$$

see calculation and discussion in Appendix F. In the numerical calculations the factor $(1 + z_N)$ was omitted – because smaller values of k^r and k^ϑ result in smaller numerical steps of r and ϑ which improves the numerical precision. The actual value of $1 + z$ at the endpoint of Downray 1 was then calculated using (3.19).

The initial t on Downray 1 is

$$t_N = t_1 + \Delta t_N = -0.013926900571845113 \text{ NTU}. \quad (7.6)$$

Note that this is the same as t_1 of (5.1) – with $\Delta t_N \approx 10^{-18}$, the Fortran program does not see the difference. This confirms the remark made under (6.6) – if determined by direct numerical calculation, the path of Backray N would become, at some point along the way, indistinguishable from that of Ray 0.

Summarizing, the initial point of Downray 1 is $(t, r, \vartheta)_{S1} = (t_N, r_1, \varepsilon)$, with the numbers given in (7.6), (5.1) and (7.2), respectively, while its initial direction is determined by (7.3) – (7.5).
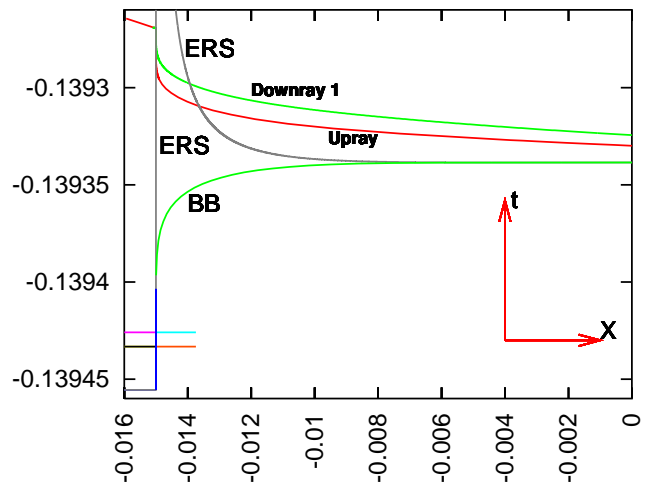

FIG. 10: Comparison of the (t, X) profiles of Downray 1 and Upray. Explanation in the text.

If continued from these initial data without corrections, Downray 1 would have the (t, X) profile shown in Fig. 10. The t-coordinate along it disagrees with that of the Upray by much more than should be expected, see Appendix G for details. This happens in consequence of a numerical instability at the outer branch of the ERS, which this author was not able to overcome. Therefore, somewhere along the way the t-coordinate of Downray 1 had to be hand-corrected. This was done as follows. At the point of closest approach of Downray 1 to the $r = 0$ line (see Appendix G), the tangent vector to the ray was parallel-transported from the actual time calculated along the ray ($t_o = -0.13932447906821049$ NTU) to the initial time of the Upray,

$$t_o' = -0.13932991589546649, \quad (7.7)$$

which is by $5.43682725598348959 \times 10^{-6}$ NTU earlier. The parallel transport was done as in Appendix B: z

was thereby unchanged, while k^r and k^ϑ were multiplied by $\mathcal{R}(t_o)/\mathcal{R}(t'_o) = 1.3849964189634454$. From there on, the ray was continued as Downray 2, see Figs. 11 – 12. Consequences of other possible modifications of Downray 1 will be discussed in Sec. VIII.
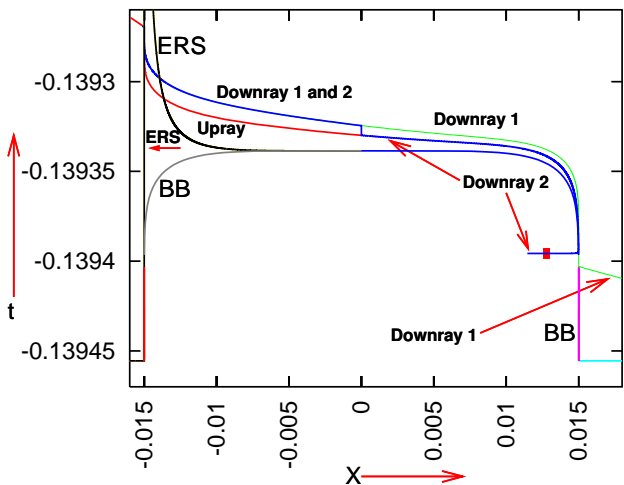

FIG. 11: The (t, X) profiles of Downray 1, Downray 2 and Upray. The small square near the lower end of Downray 2 marks its intersection with the last scattering hypersurface.
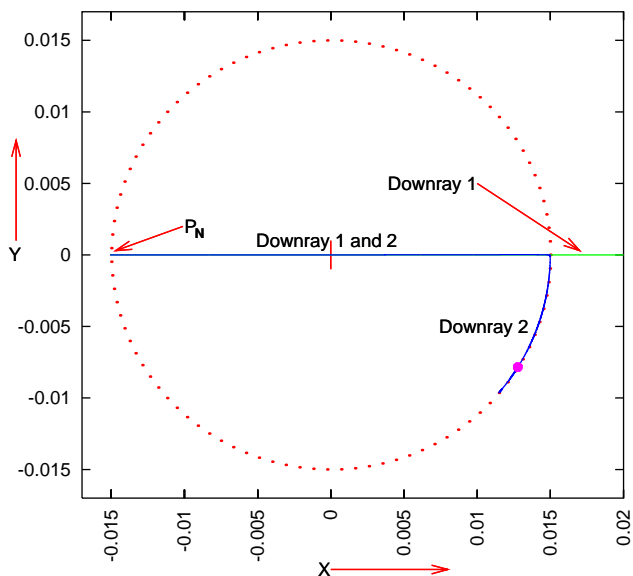

FIG. 12: Projection of Downrays 1 and 2 on the (X, Y) coordinate plane. The dot marks the intersection of Downray 2 with the last scattering hypersurface, the vertical stroke marks the origin at $r_{S1} = 0$. More explanation in the text.

The operation described above was done under two assumptions: (1) that the the point of closest approach to $r = 0$ and the direction of Downray 1 there were determined correctly, and (2) that the parallel transport could be done by the Friedmannian rule of Appendix B.

The first assumption is justified by the fact that Down-

ray 1 proceeds close to the $\vartheta = 0$ axis, with $|Y| < 4.404 \times 10^{-17}$ all the way between P_N and $X = 0$, see Fig. 13. This means that any departure from this path is smaller than the accuracy of the numerical code.

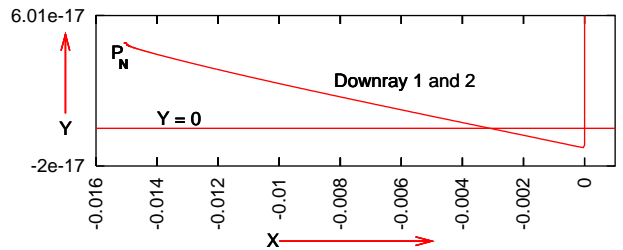
FIG. 13: Closeup view on Fig. 12 in the range $X \in [-0.016, 0.001]$. In this range Downrays 1 and 2 coincide.

The second assumption is justified by the fact that at the closest approach to the origin $r \approx 2.23 \times 10^{-22}$, $\mathcal{E},_r / \mathcal{E} \approx 2.23 \times 10^{-19}$ and $\Phi \approx 2.15 \times 10^{-25}$, so the term in (2.1) that is responsible for the difference between the QSS and Friedmann geometries is $\Phi \mathcal{E},_r / \mathcal{E} \approx 4.79 \times 10^{-44}$. The Friedmann term $\Phi,_r$ is at this location 9.62×10^{-4}. The non-Friedmannian correction is thus too small to show up at the level of accuracy assumed here.

Near the origin some quantities become indeterminate of the type 0/0 [2], so the integration of the ray equations had to include certain precautions: (1) The numerical step had to be gradually decreased on approaching the origin. (2) Downray 1 aimed at $r = 0$ with high precision, and at a certain step its r-coordinate shot to $r < 0$. This had to be taken care of. See Appendix G for details.

Figure 11 shows the (t, X) profiles of Downrays 1 and 2 across the full diameter of the BB hump. Only the left half of the ERS is shown. Downray 1 at first goes along the steep slope of the BB hump, but then turns away and crosses the LSH in the Friedmann region at

$$\begin{pmatrix} t \\ r \\ \vartheta \\ 1 + z_P \\ 1 + z_o \end{pmatrix}_{D1LSH} = \begin{pmatrix} -0.13945067585653098 \text{ NTU} \\ 0.0522717572229775690 \\ 3.1415926411632658 \\ 3.9974477620254634 \\ 335.740919327408696 \end{pmatrix}$$
(7.8)

($\vartheta_{D1LSH} = 179.999999288° \approx \pi$). The z_P is relative to the point P_N, z_o is relative to the present observer calculated from $1 + z_o = (1 + z_N)(1 + z_P)$ using (6.24).

Downray 2 never leaves the QSS1 region and finally hits the BB at the steep slope – tangentially to a surface of constant r, as predicted in (3.18). It crosses the LSH at the point marked with the small square in Fig. 11 and with the dot in Fig. 12, at

$$\begin{pmatrix} t \\ r \\ \vartheta \\ 1 + z_P \\ 1 + z_o \end{pmatrix}_{D2LSH} = \begin{pmatrix} -0.13939573683235620 \text{ NTU} \\ 0.0149934194406606183 \\ 3.6918768830001061 \\ 0.0268536489146646434 \\ 2.2554062768632145161 \end{pmatrix}.$$
(7.9)

Figure 12 shows the projection of Downrays 1 and 2 on the (X, Y) coordinate plane. At this scale, both rays seem to proceed across the QSS1 region along the symmetry axis. Figures 13 and 14 show details of the rays' paths. Downray 1 proceeds along a nearly straight line at the angle ε of (7.2) to the $Y = 0$ line and intersects it at $X \approx -0.0030588$. At $(X, Y) \approx (-4.322714809677376 \times 10^{-5}, -1.02236722643458 \times 10^{-17})$ it turns upwards and aims at $r = 0$. After reaching $(X, Y) \approx (-2.230943471939892 \times 10^{-22}, -1.07257712221974956 \times 10^{-25})$, the Fortran program finds the next r to be negative, see Appendix G to see how this problem was handled. On the other side of the origin, the two rays proceed at different angles. Downray 1 stays within the $0 \leq Y < 2.5 \times 10^{-10}$ strip up to the boundary of the QSS1 region; see the upper panel of Fig. 14. Downray 2 is initially inclined to the $Y = 0$ line at an angle that is $\approx 10^{12}$ times greater than in the $X < 0$ sector. On approaching the boundary of the QSS1 region, it bends around and becomes nearly tangent to a constant-r surface. It continues this way up to the intersection with the BB; see the lower panel of Fig. 14 and Fig. 12.
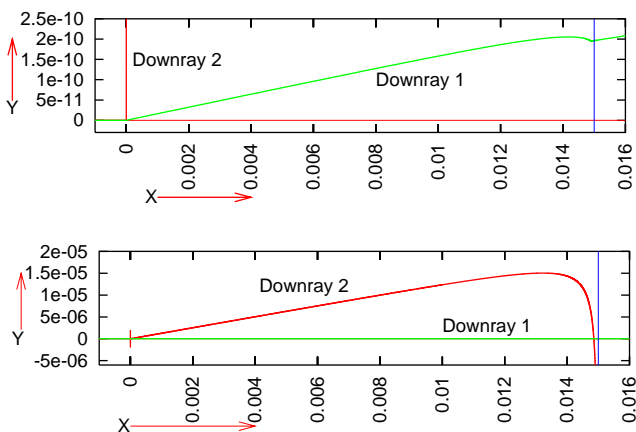

FIG. 14: Prolongation of Downray 1 and Downray 2 to the range $X \in [-0.001, 0.016]$. Note the different Y-scales in the upper and lower panels, and in Fig. 13. The thin vertical line at right is the border of the QSS1 region.

Finally, Fig. 15 shows the $\{X, z\}$ relation along Downray 2, with z relative to the present observer. The observer would see blueshift if the light sources were placed between $X \approx 0.0135$ and $X \approx 0.0149$, but will not see any blueshift in the light emitted at the LSH. For z at LSH given by (7.9), and with the parameters of the spatially flat ΛCDM model ($H_0 = 69.6$ km/(s × Mpc), $\Omega_m = 0.286$, $\Omega_\Lambda = 0.714$ [26]) the Cosmology Calculator of Refs. [25, 26] says the source of Downray 2 would be 8.726 Gyr to the past of the present observer. In the model used here, it is ≈ 0.139 NTU $= 13.622$ Gyr to the past. With $1 + z_o$ given by (7.9), the whole range of visible light is moved into near ultraviolet.

Assuming that the approximations were all valid, Eqs. (7.9) and (5.8), and Fig. 15 prove that 10 minutes after seeing a gamma-ray flash the present observer will see
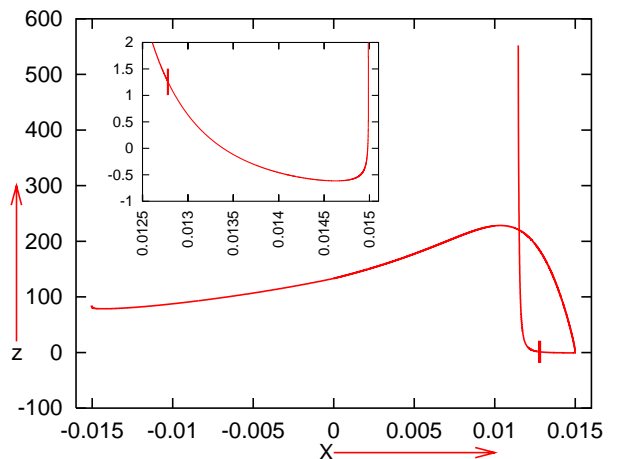

FIG. 15: The redshift along Downray 2 seen by the present observer. **Inset:** Closeup view on the neighbourhood of the minimum of z. The vertical strokes mark z at the intersection with the last scattering hypersurface, see the last line of (7.9).

radiation coming from the same direction with frequency $(1 + z_o)_{D2LSH}/(1 + z_3) \approx 1.449 \times 10^5$ times smaller. This will be in the ultraviolet range.

VIII. PERTURBATIONS OF DOWNRAY 2

Since the numerical calculations involved approximations, and they proceeded at the borderline of numerical accuracy, it is useful to investigate the redshift along rays propagating in proximity of Downray 2. For each ray described below, the numerical step on approaching the minimum r and the jump through $r = 0$ were handled in the same way as described in Appendix G.

Four sets of rays were considered:

1. Downrays 3 and 4 had the same initial $(t, r, \vartheta = \varepsilon)$ and the same initial direction as Downray 2, but the corrected t at closest approach to $r = 0$ larger (ray 3) and smaller (ray 4) than the t'_o of (7.7).

In the next three sets, the corrected t at closest approach to $r = 0$ was (7.7).

2. Downrays 5 – 7 had the same initial $(t, r, \vartheta = \varepsilon)$ as Downray 2, but $\widetilde{\gamma}_N$ zero, minus that of Downray 2 and twice that of Downray 2, respectively ($\widetilde{\gamma}_N = 0$ means that the initial direction is parallel to the $Y = 0$ line).

3. Downrays 8 – 10 had the same initial (t, r) as Downray 2, but ε twice as large, and the same values of $\widetilde{\gamma}_N$ as Downrays 5, 6 and 2, respectively.

4. Downrays 11 – 13 had the same initial (t, r) as Downray 2, but half the value of ε, and the same set of values of $\widetilde{\gamma}_N$ as in point 3.

For Downray 3 trial time-intervals $\tau_n = 10^{-n}$ NTU were added to the t'_o of (7.7) to verify the effect. With $n = 18$ the effect was invisible, as expected. With $n = 17, 16, \ldots, 8$ the changes in $(t, r, \vartheta, 1 + z_P)$ at the LSH compared to those of Downray 2 were small and

qualitatively insignificant. Only at $n = 7$ a substantial change occurred. The ray hit the BB at the boundary of the QSS1 region at earlier t than Downray 2, but the program could not detect its intersection with the LSH. The ray with $\tau_{7.2} = 2 \times 10^{-7}$ NTU (Downray 3 in the figures) flew over the BB hump and intersected the LSH in the Friedmann region, with $(r, 1 + z_o) \approx (0.03724, 8.0629)$.

For Downray 4, the trial intervals added to t'_o were $\widetilde{\tau}_n = -10^{-n}$ NTU. Similarly to Downray 3, a noticeable difference occurred only at $n = 6$: the ray hit the LSH well before reaching the edge of the QSS1 region, with $(r, 1 + z_P) \approx (0.0145, 182.256)$.

The conclusion is that the value of $1 + z$ at the LSH is not sensitive to the values of τ_n and $\widetilde{\tau}_n$ as long as $\tau \leq 10^{-8}$ NTU $= 980$ years, i.e., it is not sensitive to numerical errors smaller than 10^{-8} NTU.

Details of the other results are described in Appendix H. Here is just a short summary:

On rays 5 to 9 and 12, $1 + z_o$ was sufficient to move the whole visible light range into the ultraviolet; see Table II in Appendix H and Ref. [27] for the numbers. On Downray 10, the visible range was moved into the near ultraviolet just adjacent to the visible range. On rays 11 and 13, the visible range was slightly shifted toward violet (Downray 11) or toward red (Downray 13), but most of it remained visible.

The final conclusion is that the result calculated in Sec. VII remains valid for past-directed rays that reach the neighbourhood of the point P_N with directions close to that of Downray N: on all those rays, the present observer would see redshift or only weak blueshift ($1 + z \approx 0.91$ on Downray 11). A strong blueshift $1 + z \approx 10^{-5}$ would only be seen on Ray 0 that goes along the symmetry axis of the QSS1 region.

In fact, this result was to be expected on the basis of the comments to eq. (3.17), but it is instructive to have it confirmed by explicit computations.

IX. CONCLUSIONS AND PROSPECTS

The present paper is a continuation and development of Ref. [3]. In that paper, it was shown that if a light ray is emitted at the last-scattering hypersurface in an axially symmetric quasispherical Szekeres region (denoted QSS1) along the symmetry axis, with the frequency in the visible range, then it will follow this axis all through QSS1 and might be blueshifted by so much that the present observer will see it as a gamma ray. The axial direction is unstable, and rays proceeding in a close neighbourhood of the symmetry axis will be now observed in the ultraviolet range.

In the present paper, it was investigated what happens to the maximally blueshifted ray (MBR) if, on its way between the emission point and the present observer, it passes through another QSS region (denoted QSS2). Both QSS regions are matched into a Friedmann background of negative spatial curvature, and the observer is in this background.

The QSS metrics and some of their properties were introduced in Secs. II – IV. In Sec. V, it was shown that if the MBR passes through QSS2 along a generic path,[7] then is deflected by a continuously changing angle via the cosmic drift effect [10, 12]. Therefore, any observer can find herself in this ray's path only at a single instant of time. At all other times, the rays coming from the same direction will have lower frequencies (i.e. will be redshifted or only slightly blueshifted), while the MBR will miss the observer. The rate of angular drift of the MBR was calculated in Sec. VI. Using this result, in Sec. VII it was demonstrated by a numerical calculation that an MBR that reached a present observer at some instant will no longer be visible to her after 10 minutes. Instead, the ray coming from the same direction will be in the ultraviolet range. Finally, in Sec. VIII (with numerical details in Appendix H) it was shown that the result of Sec. VII is not sensitive to perturbations smaller than 10^{-8} NTU $= 980$ years of the instant when the rays cross the origin of the QSS1 region, and smaller than $\approx 3.3 \times 10^{-15}$ rad $= 1.89 \times 10^{-13}$ ° of their direction on exit from the QSS1 region.

It follows that, in the present model, the gamma-ray flash is instantaneous. As any model, this one is an idealisation. In reality, mechanisms should exist that will stretch the instant of observation of the gamma ray to a short but finite interval. Modelling them may require using more general metrics and other BB profiles than those used here. Refs. [1–3] and the present paper provided a proof of existence of a mechanism that can shift the range of visible light frequencies to the gamma range, and that will ensure short-livedness of the high-frequency flash.

The two QSS regions were assumed axially symmetric for simplicity. Then the MBR must follow the symmetry axis in the QSS1 region, so in the numerical calculations it can be kept on this path, even though this direction is unstable [2, 3]. But strong blueshifts are generated also by fully nonsymmetric QSS regions [2]. In the nonsymmetric case, the MBR will be changing its direction with time in consequence of the cosmic drift within the source [10, 12], even in the absence of the deflecting region. This process is a more difficult numerical challenge: the maximally blueshifted ray must be identified by numerics alone [2].

The model presented here does not solve the problem of too-long-lasting afterglows. This will be the subject of a separate paper.

———————

[7] Non-generic paths are along the symmetry axis and in the plane of the Szekeres dipole equator.

APPENDIX A: CALCULATING δ IN (5.5)

The unit vector tangent to the line $(t, \vartheta, \varphi) = (t_1, \pi/2, \text{constant})$ in the Friedmann region is, using (3.3):

$$n_2^\alpha = \left(0, \frac{\sqrt{1+2E}}{\mathcal{N}}, 0, 0\right). \qquad (A1)$$

The unit direction vector of a null vector k^α is [24]

$$n_1^\alpha = u^\alpha - \frac{k^\alpha}{k^\rho u_\rho}. \qquad (A2)$$

In our case $u^\alpha = \delta_0^\alpha$. Consequently, at the initial point of the ray, using (3.15), eq. (A2) becomes

$$n_1^\alpha = \left(0, \frac{k_i^r}{1+z_1}, \frac{k_i^\vartheta}{1+z_1}, 0\right), \qquad (A3)$$

where z_1 is given by (5.2) (account was taken of $k^\varphi = 0$). From (3.17) with $J_0 = 0$ we have, again using (3.15)

$$k_i^r = \pm\frac{\sqrt{1+2E_i}}{\mathcal{N}_i}\sqrt{(1+z_1)^2 - \left(\frac{\Phi_i k_i^\vartheta}{\mathcal{F}_i}\right)^2}. \qquad (A4)$$

So, the angle between n_1^α and n_2^α is given by

$$\cos\delta = -g_{\alpha\beta}n_1^\alpha n_2^\beta = \sqrt{1 - \left[\frac{k_i^\vartheta \Phi_i}{\mathcal{F}_i(1+z_1)}\right]^2}. \qquad (A5)$$

Since the initial point of Ray 0 is in the Friedmann region, where $\mathcal{F} \equiv 1$, the above is equivalent to (5.5).

APPENDIX B: PARALLEL TRANSPORT ALONG u^α IN A FRIEDMANN REGION

In a Friedmann region a vector k^μ parallel-transported along $u^\alpha = \delta_0{}^\alpha$ obeys $k^t = \text{constant}$, $k^i\mathcal{R} = \text{constant}$, $i = 1, 2, 3$, i.e., the ratio k^ϑ/k^r stays constant. Then

$$k_{\ell t}^t = k_{et}^t, \qquad (B1)$$

$$(k^r, k^\vartheta)_{et} = \frac{\mathcal{R}(t_{\ell t})}{\mathcal{R}(t_{et})}(k^r, k^\vartheta)_{\ell t}, \qquad (B2)$$

where ℓt and et denote "at a later time" and "at an earlier time", respectively. If k^μ is a null vector and we wish to reset z from $z_{\ell t}$ to z_{et}, then (B2) is modified as follows:

$$(k^r, k^\vartheta)_{et} = \frac{\mathcal{R}(t_{\ell t})}{\mathcal{R}(t_{et})}(k^r, k^\vartheta)_{\ell t} \times \frac{1+z_{et}}{1+z_{\ell t}}. \qquad (B3)$$

APPENDIX C: CALCULATING THE ANGLES FOR (6.1) − (6.5)

The direction of Ray 0 in the (X, Y) surface at the future endpoint can be read off from the table of values of X and Y found by the same program that calculated the path of the ray. The last two pairs in this table are

$$(X, Y)_1$$
$$= (0.38875803859076119, -0.75833536622992936),$$
$$(X, Y)_2 \qquad (C1)$$
$$= (0.38875804873013375, -0.75833538643402199).$$

Hence the final direction of Ray 0 in the (X, Y) surface is inclined to the $Y = 0$ line at the angle β_0, where

$$|\tan\beta_0| \overset{\text{def}}{=} \left|\frac{dX}{dY}\right|_{r_{\text{fin}}} = \frac{X_2 - X_1}{|Y_2 - Y_1|}$$
$$= 0.50184745960551459,$$
$$\implies \beta_0 = 26.64966989421893587°. \quad (C2)$$

In the same way we find for Ray 2:

$$\beta_2 = 28.44458627797032091 \qquad (C3)$$

So, $\Delta\beta = \beta_2 - \beta_0$ is as given by (6.1).

APPENDIX D: CORRECTING THE DIRECTION OF BACKRAY 0 IN SEC. VII

The value of $\mu = k^\vartheta/k^r$ at $t = t_{\text{fin}}$ of (5.9), as calculated by the program that determined Ray 0, was

$$\mu \overset{\text{def}}{=} k^\vartheta/k^r = 0.0100796385641537794. \qquad (D1)$$

But when the initial direction of Backray 0 had this μ, its path at entry to QSS2 visibly differed (at the scale of the insets in Fig. 3) from that of Ray 0. This had to be caused by numerical errors because there is no cosmic drift in the Friedmann region [10]. Consequently, the μ in (D1) had to be corrected by trial and error. With μ given in (6.8) the two rays coincide at the edge of QSS2 up to the level of accuracy[8] shown in Fig. 16.

APPENDIX E: CALCULATING THE ANGLE γ IN FIG. 8

Let ϑ be the parameter along the arc SF. The unit tangent vector to SF at $(r, \vartheta) = (r_b, \vartheta_b)$ is

$$n_{\text{SF}}^\alpha = \frac{1}{\mathcal{R}(t_b)\ell}\left(0, \frac{dr}{d\vartheta}\bigg|_{\vartheta=\vartheta_b}, 1, 0\right), \qquad (E1)$$

where $\mathcal{R}(t_b)$ is given by (6.15), and $dr/d\vartheta|_{\vartheta=\vartheta_b}$ is found by taking (6.9) at $(r, \vartheta) = (r_b, \vartheta_b)$:

$$\frac{dr}{d\vartheta}\bigg|_{r=r_b} = -r_b\cot(\vartheta_b + \delta). \qquad (E2)$$

———

[8] See footnote 6 – the irregularity of Backray 0 at the edge of QSS2 is an interpolation by the drawing program.
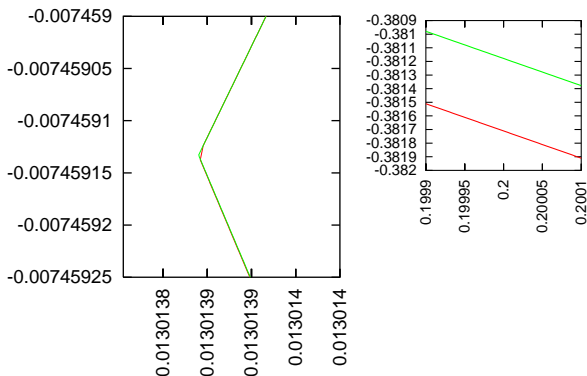
FIG. 16: **Left panel:** Paths of Ray 0 (red) and of corrected Backray 0 (green) coincide at the edge of QSS2 to better than 10^{-8} in both X and Y. **Right panel:** The same paths midway between QSS2 and the present observer. The coincidence is only up to $\Delta Y \approx 5 \times 10^{-4}$.

The normalizing factor ℓ is

$$\ell = r_b \sqrt{\frac{\cot^2(\vartheta_b + \delta)}{1 - k r_b^2} + 1}. \qquad \text{(E3)}$$

The unit direction vector of Backray 0 at the same point is calculated by analogy to (A3), it is

$$n_{\mathrm{ray}}^\alpha = \left(0, \frac{k_b^r}{1 + z_b}, \frac{k_b^\vartheta}{1 + z_b}, 0\right), \qquad \text{(E4)}$$

where z_b is given by (6.14). Consequently, the angle γ between n_{SF}^α and n_{ray}^α is given by

$$\cos \gamma = \frac{r_b \mathcal{R}(t_b)}{\ell (1 + z_b)} \left[-\frac{k_b^r \cot(\vartheta_b + \delta)}{1 - k r_b^2} + r_b k_b^\vartheta\right]. \qquad \text{(E5)}$$

The values given in (6.16) were calculated from (E5).

APPENDIX F: CALCULATING (7.3) − (7.5)

In the coordinates of the QSS1 region, the line OL obeys the equation $X \equiv -r \cos \vartheta = $ constant, so the unit tangent vector to it, n_{OL}^α, obeys $n_{\mathrm{OL}}^r = r \tan \vartheta \, n_{\mathrm{OL}}^\vartheta$, $n_{\mathrm{OL}}^t = n_{\mathrm{OL}}^\varphi = 0$ and $g_{\alpha\beta} n_{\mathrm{OL}}^\alpha n_{\mathrm{OL}}^\beta = -1$. The angle γ_N in Fig. 9 is between the initial direction of Downray 1 and the unit tangent vector to OL pointing *downward*, so

$$n_{\mathrm{OL}}^r = -\frac{\tan \vartheta}{\mathcal{R}(t)\ell_{\mathrm{OL}}}, \qquad n_{\mathrm{OL}}^\vartheta = -\frac{1}{r\mathcal{R}(t)\ell_{\mathrm{OL}}},$$

$$\ell_{\mathrm{OL}} = \sqrt{\frac{\tan^2 \vartheta}{1 - k r^2} + 1}. \qquad \text{(F1)}$$

The unit direction vector of Downray 1 at P_N is, similarly to (A3) and (E4),

$$n_N^\alpha = \left(0, \frac{k_N^r}{1 + z_N}, \frac{k_N^\vartheta}{1 + z_N}, 0\right). \qquad \text{(F2)}$$

At P_N, $-g_{\alpha\beta} n_{\mathrm{OL}}^\alpha n_N^\beta = \cos \gamma_N = \sin \widetilde{\gamma}_N$, so

$$\frac{\tan \varepsilon}{1 - k r_1^2} \, k_N^r + r_1 k_N^\vartheta = -\frac{\ell_N}{\mathcal{R}_N} \, (1 + z_N) \sin \widetilde{\gamma}_N, \qquad \text{(F3)}$$

where $\mathcal{D}$ is given by (7.5) and

$$\ell_N \overset{\mathrm{def}}{=} \ell_{\mathrm{OL}}(r_1, \varepsilon) = \frac{\mathcal{D}}{\sqrt{1 - k r_1^2}},$$

$$t_N \overset{\mathrm{def}}{=} t_1 + \Delta t_N, \quad \mathcal{R}_N \overset{\mathrm{def}}{=} \mathcal{R}(t_N). \qquad \text{(F4)}$$

The vector k^α obeys $g_{\alpha\beta} k^\alpha k^\beta = 0$. Since Downray 1 prolongs Backray N, Eq. (3.15) continues to hold along it. Consequently, at $(r, \vartheta) = (r_1, \varepsilon)$ we have

$$(1 + z_N)^2 - \frac{\mathcal{R}_N^2}{1 - k r_1^2} (k_N^r)^2 - (r_1 \mathcal{R}_N)^2 (k_N^\vartheta)^2 = 0. \qquad \text{(F5)}$$

Solving the set (F3), (F5) for k_N^r and k_N^ϑ we obtain

$$k_N^r = \frac{\sqrt{1 - k r_1^2} (1 + z_N)}{\mathcal{R}_N \mathcal{D}}$$
$$\times \left(-\tan \varepsilon \sin \widetilde{\gamma}_N \pm \sqrt{1 - k r_1^2} \cos \widetilde{\gamma}_N\right), \qquad \text{(F6)}$$

$$k_N^\vartheta = \frac{1 + z_N}{r_1 \mathcal{R}_N \mathcal{D}}$$
$$\times \left(-\sqrt{1 - k r_1^2} \sin \widetilde{\gamma}_N \mp \tan \varepsilon \cos \widetilde{\gamma}_N\right). \qquad \text{(F7)}$$

The double sign in (F6) follows from the ambiguity in the definition of k_N^r: its direction is given only by the angle it forms with OL, so it can point away from QSS1 or into QSS1. We need to follow the second possibility, which corresponds to the lower sign and implies $k_N^r < 0$. The upper sign would correspond to $k_N^r > 0$ because $\sqrt{1 - k r_1^2} \cos \widetilde{\gamma}_N \gg \tan \varepsilon \sin \widetilde{\gamma}_N$. This is because $\sqrt{1 - k r_1^2} > 1$, $\cos \widetilde{\gamma}_N \approx 1$ while $\sin \widetilde{\gamma}_N$ and $\tan \varepsilon$ are both tiny in consequence of (7.2) and (6.22).

The situation with the sign of k_N^ϑ is less clearcut. The double sign in (F7) is coupled with that in (F6), and having chosen "−" in (F6) we have to choose "+" in (F7) – but then k_N^ϑ might still be positive or negative, depending on the numerical values of the quantities in it. Since $\pi/2 - \gamma_N = \widetilde{\gamma}_N > \varepsilon$ as seen from (6.22) and (7.2), and ϑ increases clockwise, the initial direction of Downray 1 is toward decreasing ϑ, so $k_N^\vartheta < 0$ follows. This is qualitatively reflected in Fig. 9. The Fortran 90 program, using (F7), found $k_N^\vartheta = -3.39090742613403823 \times 10^{-12}$.

Equations (7.3) – (7.4) are (F6) – (F7) with the signs already chosen.

APPENDIX G: NUMERICAL CALCULATIONS OF DOWNRAYS 1 AND 2

The difference of the t-coordinates of Upray and Downray 1 at the smallest r ($\approx 2.23 \times 10^{-22}$) is $\approx 5.437 \times 10^{-6}$ NTU. Since Downray 1 is supposed to represent the

ray that reaches the observer 10 min later than Up-ray, their time-difference at $r = 0$ should be 10 min $\times (1 + z)_{3 \text{ up}} = 7.19 \times 10^{-2}$ min $= 1.395 \times 10^{-18}$ NTU, where $(1+z)_{3 \text{ up}}$ is the upward $1+z$ between the origin of QSS1 and the present observer given by (5.6). So clearly, the difference found by the Fortran program is unrealistically large. If Downray 1 were continued uncorrected, it would fly above the BB hump and intersect the LSH in the Friedmann region with $1 + z$ as given in (7.8); part of its path is shown in Fig. 11. Formally, this would mean that the gamma-ray flash is no longer visible on this ray, but this would not prove the intended point of this paper. It is known that the high-frequency flash will end if the observer simply waits long enough, but the time-scale of this process is too long [1]. What we wish to show here is that 10 min after the observer saw the gamma flash, the ray coming from the same direction will be emitted off the symmetry axis of QSS1 and will have a lower frequency for this reason. Therefore, the t-coordinate along Downray 1 had to be decreased by hand.

TABLE I: Changes in $\Delta\lambda$ in a vicinity of $r = 0$. The initial value was $\Delta\lambda = 10^{-12}$. r in the last line is the closest approach to $r = 0$

At $r = $	$\Delta\lambda$ was multiplied by
0.0149	100
2×10^{-6}	1/1000
10^{-10}	1/1000
2×10^{-13}	1/100
2×10^{-15}	1/100
5×10^{-17}	1/100
2×10^{-19}	1/100
$\approx 2.23 \times 10^{-22}$	1/1000

Downray 1 runs near to the symmetry axis of QSS1 and is nearly parallel to it. When the ray approaches $r = 0$, at a certain step the next r becomes negative. In an attempt to prevent this, the step $\Delta\lambda$ in the affine parameter λ was gradually decreased on approaching the origin. Table I shows the reductions in $\Delta\lambda$ and the values of r at which they were done. But the jump to $r < 0$ persisted. So, when the Fortran program reached the limit of its precision, the jump to $r < 0$ was interpreted as the jump from the last (r, ϑ) where r was still positive to $(r, \pi + \vartheta)$ (see Figs. 17 and 18), and the program continued from there. (As the ray was receding from the origin and passed through the values of r from Table I in a reverse order, $\Delta\lambda$ was multiplied by the reverse of the factor from the table at each border value of r. In addition, at $r = 0.01$ and $X > 0$, $\Delta\lambda$ was multiplied by 100.) Figures 11 – 14 show the resulting graphs.

In order to locate the intersections of Downray 2 with the LSH and with the BB with a greater precision, more modifications of $\Delta\lambda$ were made. It was multiplied by
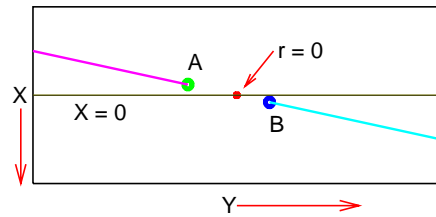

FIG. 17: When the ray passes near $r = 0$, at the point A of coordinates (r_A, ϑ_A) the numerical program jumps to (r_B, ϑ_B) with $r_B < 0$. This is interpreted as the jump to point B of coordinates $(r, \vartheta) = (-r_B, \vartheta_A + \pi)$. This graph is a sketch; for the real situation see Fig. 18.
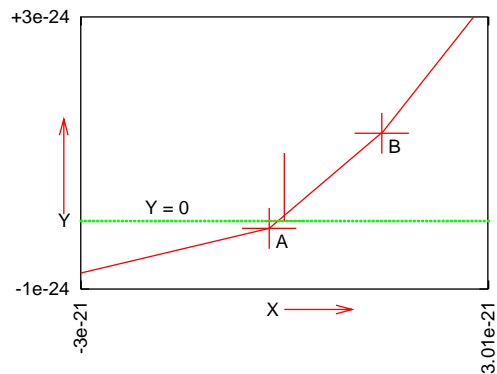

FIG. 18: The situation from Fig. 17 in real scale for Downray 2. The segment AB is an interpolation by the plotting program. The (X, Y) coordinates of points A and B are $(-2.23 \times 10^{-22}, -1.073 \times 10^{-25})$ and $(1.4367 \times 10^{-21}, 1.29 \times 10^{-24})$, respectively. The longer vertical stroke marks $X = 0$.

1/100 at step 114,685,150, and then again by 1/1000 at step 115,226,000. The LSH and BB were reached in steps 114,698,353 and 115,634,944, respectively, but the last number is not reliable. Since the ray becomes tangent to a surface of constant r when approaching the BB, it is difficult to locate the intersection point – the result strongly depends on the value of $\Delta\lambda$. But the exact point where the ray hits the BB has no physical meaning because the QSS metric does not apply at times before the LSH.

APPENDIX H: DETAILS FOR SEC. VIII

Table II gives the redshifts/blueshifts on Downrays 5 to 13 between the LSH and the point P_N $(1 + z_P)$, and between the LSH and the present observer $(1 + z_o)$.

Figure 19 shows where Downrays 3 to 13 intersect the LSH; the intersection points are marked with dots. Four typical examples of the rays are displayed in full. Downray 3 escapes from the QSS1 region and intersects the LSH in the Friedmann region, beyond Fig. 19. Downray 4 intersects the LSH between $r = 0$ and the boundary of the QSS1 region, and hits the BB still inside QSS1. Downray 7 turns toward $Y < 0$ near the boundary of the

TABLE II: Redshift from the LSH on Downrays 5 to 13

ray	$1 + z_P$	$1 + z_o$
5	0.070480436257171	5.91956865287204
6	0.110226238143066	9.25777164112425
7	0.024772171188802	2.08058541944529
8	0.113160537766071	9.50422000309368
9	0.104598722390451	8.7851232352436
10	0.020657768217553	1.73502157013793
11	0.011190786419531	0.939900942842124
12	0.330430215246075	27.7524437702868
13	0.012570655453927	1.05579451437558

QSS1 region, and intersects the LSH near the steep slope of the BB hump. Downray 12 turns toward $Y > 0$, and intersects the LSH near another point of the steep slope of the BB hump. Downray 13 follows a part of the path of Downray 7, the other rays follow parts of the path of Downray 12. They intersect the LSH at various ϑ, but at r nearly on the boundary of the BB hump.
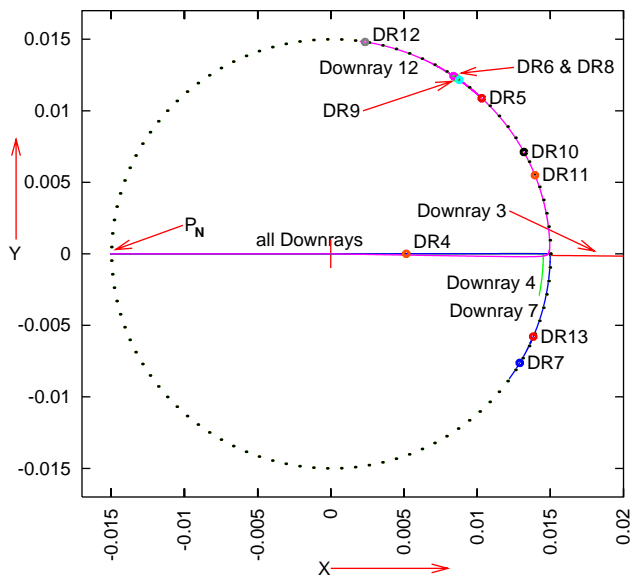

FIG. 19: The intersections of Downrays 3 to 13 with the LSH projected on the (X, Y) coordinate plane (marked with large dots). Projections of selected rays are shown in full; the remaining ones follow parts of the paths of Downray 7 or Downray 12. Downray 3 intersects the LSH in the Friedmann region beyond the right margin of the figure.

Figures 20 and 21 show the rays between their initial points and the neighbourhood of $r = 0$. In this segment, they stay within the strip $-2 \times 10^{-16} < Y < 6 \times 10^{-16}$ and pass through $r = 0$ in ways similar to that shown in Figs. 17 and 18.

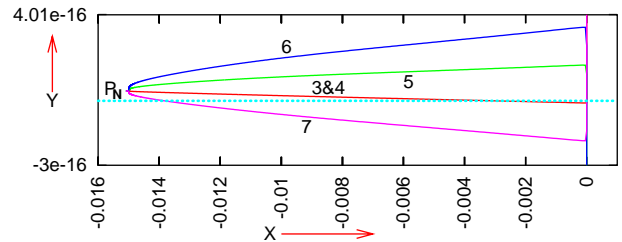Figures 22 and 23 show the rays between $r = 0$ and

FIG. 20: Downrays 3 to 7 in the segment $X \in (-r_1, 0)$. Near to $r = 0$ they all begin to aim at $r = 0$. The passage through $r = 0$ is handled as described in Appendix G. The dotted horizontal line marks $Y = 0$.
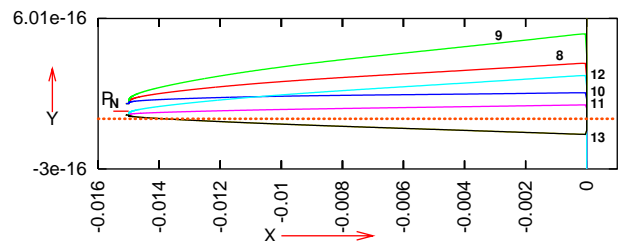

FIG. 21: Downrays 8 to 13 in the segment $X \in (-r_1, 0)$. Near to $r = 0$ they behave just as those in Fig. 20. The short horizontal dash marks the Y coordinate of the point P_N.

$r = r_F$ given by (2.23). Here they depart from the $Y = 0$ line much further than in the $X < 0$ segment: most stay in the strip $-7 \times 10^{-5} < Y < 2 \times 10^{-5}$, except for Downray 12 that at the farthest distance from the $Y = 0$ axis has $Y \approx -1 \times 10^{-4}$. Close to the boundary of QSS1 they bend around and become nearly tangent to surfaces of constant r. Downray 3 is an exception: it follows the nearly-constant-r path for a short while, then escapes to larger r, as seen in Fig. 19. Downray 4 hits the BB at r distinctly smaller than the r_F of (2.23), the remaining rays hit it at r very close to r_F.

[1] A. Krasiński, Cosmological blueshifting may explain the gamma ray bursts. *Phys. Rev.* **D93**, 043525 (2016).
[2] A. Krasiński, Existence of blueshifts in quasi-spherical Szekeres spacetimes. *Phys. Rev.* **D94**, 023515 (2016).
[3] A. Krasiński, Properties of blueshifted light rays in quasisispherical Szekeres metrics. ArXiv 1704.08145, accepted
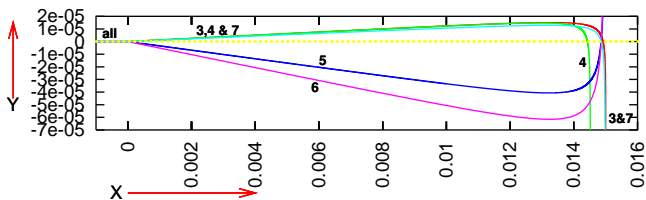
FIG. 22: Downrays 3 to 7 in the segment $X \in (-0.001, 0.016)$. At the scale of this figure, all rays coincide for $X < 0$. The dotted horizontal line marks $Y = 0$.
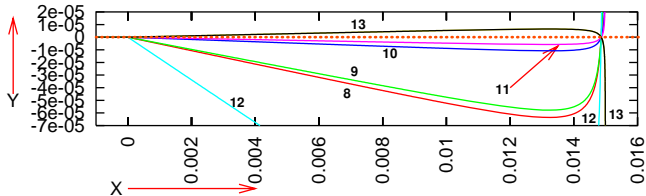

FIG. 23: Downrays 8 to 13 in the segment $X \in (-r_1, 0)$. The minimum Y on Downray 12 is $\approx -1 \times 10^{-4}$.

for *Phys. Rev.* **D**.

[4] D. Perley, Gamma-Ray Bursts. Enigmatic explosions from the distant universe.
http://w.astro.berkeley.edu/~dperley/pub/grbinfo.html

[5] P. Szekeres, A class of inhomogeneous cosmological models. *Commun. Math. Phys.* **41**, 55 (1975).

[6] P. Szekeres, Quasispherical gravitational collapse. *Phys. Rev.* **D12**, 2941 (1975).

[7] J. Plebański and A. Krasiński, *An Introduction to General Relativity and Cosmology.* Cambridge University Press 2006, 534 pp, ISBN 0-521-85623-X.

[8] P. Szekeres, Naked singularities. In: *Gravitational Radiation, Collapsed Objects and Exact Solutions.* Edited by C. Edwards. Springer (Lecture Notes in Physics, vol. 124), New York, pp. 477 – 487 (1980).

[9] C. Hellaby and K. Lake, The redshift structure of the Big Bang in inhomogeneous cosmological models. I. Spherical dust solutions. *Astrophys. J.* **282**, 1 (1984) + erratum *Astrophys. J.* **294**, 702 (1985).

[10] A. Krasiński and K. Bolejko, Redshift propagation equations in the $\beta' \neq 0$ Szekeres models. *Phys. Rev.* **D83**, 083503 (2011).

[11] C. Quercellini, L. Amendola, A. Balbi, P. Cabella, M. Quartin, Real-time cosmology. *Phys. Rep.* **521**, 95 – 134 (2012).

[12] M. Korzyński and J. Kopiński, Optical drift effects in general relativity. arXiv:1711.00584, to be published.

[13] C. Hellaby, The nonsimultaneous nature of the Schwarzschild $R = 0$ singularity. *J. Math. Phys.* **37**, 2892 (1996). publication.

[14] W. B. Bonnor, A. H. Sulaiman and N. Tomimura, Szekeres's space-times have no Killing vectors, *Gen. Rel. Grav.* **8**, 549 (1977).

[15] M. M. de Souza, Hidden symmetries of Szekeres quasi-spherical solutions, *Revista Brasileira de Física* **15**, 379 (1985).

[16] C. Hellaby and A. Krasiński. You cannot get through Szekeres wormholes or regularity, topology and causality in quasi-spherical Szekeres models. *Phys. Rev.* **D66**, 084011 (2002).

[17] G. Lemaître, L'Univers en expansion [The expanding Universe]. *Ann. Soc. Sci. Bruxelles* **A53**, 51 (1933); English translation: *Gen. Relativ. Gravit.* **29**, 641 (1997); with an editorial note by A. Krasiński: *Gen. Relativ. Gravit.* **29**, 637 (1997).

[18] R. C. Tolman, Effect of inhomogeneity on cosmological models. *Proc. Nat. Acad. Sci. USA* **20**, 169 (1934); reprinted: *Gen. Relativ. Gravit.* **29**, 935 (1997); with an editorial note by A. Krasiński, in: *Gen. Relativ. Gravit.* **29**, 931 (1997).

[19] A. Krasiński, Blueshifts in the Lemaître – Tolman models. *Phys. Rev.* **D90**, 103525 (2014).

[20] A. Krasiński, Accelerating expansion or inhomogeneity? A comparison of the ΛCDM and Lemaître – Tolman models. *Phys. Rev.* **D89**, 023520 (2014) + erratum *Phys. Rev.* **D89**, 089901(E) (2014).

[21] Energy and Work Units Conversion,
http://www.asknumbers.com/EnergyWorkConversion.aspx

[22] Planck collaboration, Planck 2013 results. XVI. Cosmological parameters. *Astron. Astrophys.* **571**, A16 (2014).

[23] Planck collaboration, Planck 2013 results. XV. CMB power spectra and likelihood. *Astron. Astrophys.* **571**, A15 (2014).

[24] G. F. R. Ellis, Relativistic cosmology. In *Proceedings of the International School of Physics "Enrico Fermi", Course 47: General relativity and cosmology.* Edited by R.K. Sachs, Academic Press, 1971, pp. 104-182. Reprinted: *Gen. Relativ. Gravit.* **41**, 581 (2009); with an editorial note by W. Stoeger, in *Gen. Relativ. Gravit.* **41**, 575 (2009).

[25] E. L. Wright, A Cosmology Calculator for the World Wide Web. *Publ. Astr. Soc. Pac.* **118**, 1711 (2006).

[26] E. L. Wright, Ned Wright's Javascript cosmology calculator,
http://www.astro.ucla.edu/~wright/ACC.html

[27] The Electromagnetic Spectrum,
https://www.miniphysics.com/electromagnetic-spectrum_25.html

[28] A. Krasiński, The newest release of the Ortocartan set of programs for algebraic calculations in relativity. *Gen. Relativ. Gravit.* **33**, 145 (2001).

[29] A. Krasiński, M. Perkowski, *The system ORTOCARTAN – user's manual.* Fifth edition, Warsaw 2000.